INT. J. AMBIENT ENERGY

https://www.tandfonline.com/journals/taen20

ACCEPTED APRIL 13TH 2023

Computation of EMHD ternary hybrid non-Newtonian nanofluid over a wedge embedded in a Darcy-Forchheimer porous medium

[1]J. Prakash, *[2]Dharmendra Tripathi and [3]O. Anwar Bég
[1]Department of Mathematics, Avvaiyar Government College for Women, Karaikal – 609 602,
Puducherry-U.T., ***India.*** prakashjayavel@yahoo.co.in
[2]Department of Mathematics, National Institute of Technology Uttarakhand,
Srinagar- 246174, ***India****.* dtripathi@nituk.ac.in
[3]Multi-Physical Engineering Sciences Group, Dept. Mechanical and Aeronautical Engineering,
SEE, Salford University, Manchester, M54WT, **UK***.* O.A.Beg@salford.ac.uk*;*
gortoab@gmail.com

ABSTRACT

The field of engineering is witnessing an increasing number of applications for intelligent electromagnetic nano-coatings. These recent advancements serve as the impetus for an investigation into a theoretical and computational study of an unsteady electro-magneto-hydrodynamic (EMHD) incompressible two-dimensional tangent hyperbolic non-Newtonian ternary hybrid nanofluid boundary layer coating flow external to a two-dimensional porous wedge geometry adjacent to a Darcy-Forchheimer porous medium. Both aligned electrical and transverse magnetic field effects are included. The effects of zeta-potential and surface injection/suction are included. The ternary composite nanofluid comprises three nanoparticles (Al_2O_3, TiO_2 and SiO_2) with aqueous base fluid (H_2O). The governing conservation partial differential equations for continuity and momentum and associated boundary conditions at the wedge surface and free stream are transformed with appropriate similarity variables. The emerging ordinary differential nonlinear boundary value problem is numerically solved in MATLAB. Validation with earlier studies is included. A significant deceleration is induced in the flow of a ternary hybrid nanofluid with an increase in the electric field parameter. An increment in Falkner-Skan power-law constant (moving wedge angle parameter) boosts the local skin friction coefficient for both the ternary hybrid nanofluid (THNF) and unitary Al_2O_3 nanofluid (UNF) cases. Both electroosmosis and electric field parameters improve the velocity distribution for both THNF and UNF flow cases. The flow is boosted with an increase in the power-law rheological characteristic, which ranges from shear-thinning $n < 1$ to shear-thickening $n > 1$. The flow is accelerated by increasing the Darcy number, whereas it is retarded by increasing the Forchheimer number (which measures non-Darcy inertial drag) or the Weissenberg number (thicker momentum boundary layers). Greater values of the wedge surface injection parameter cause the flow to accelerate and the momentum boundary layer thickness to diminish, whereas surface suction produces the opposite effect. Electric potential magnitudes increase with an increase in the zeta potential parameter, whereas an increase in the electroosmosis parameter has the opposite effect, reducing the electric potential magnitudes.

KEYWORDS: *Wedge flow; Magnetic field; Electroosmotic flow; Darcy-Forchheimer porous medium, ternary hybrid nanofluids, non-Newtonian tangent hyperbolic model; smart coating.*

1.INTRODUCTION

Coating flows have received significant attention in the scientific literature owing to growing applications in medical, aerospace, industrial materials (polymer) processing and environmental engineering. Such flows can be simulated with boundary layer theory for a range of geometries depending on the substrate being protected. These include flat plates, curved bodies and wedges, all of which feature extensively in modern manufacturing processes. Coating transport phenomena may involve Newtonian and non-Newtonian fluids, heat transfer, mass transfer and other phenomena. For the wedge geometry, external boundary layer flows are often classified as "Falkner-Skan" flows. One of the earliest studies of viscoelastic wedge coating flow was communicated by Hsu [1] who showed that for homogeneous viscoelastic soluble coating flow on a wedge, the surface friction is elevated with shear-thickening whereas it is reduced with shear-thinning. In recent years nanomaterial coatings [2] and also electro-magnetic deposition of coatings [3] and jet electrohydrodynamic coating methods [4] have been explored. The emergence of nanofluids [5] in recent years has also impacted on the evolution of new smart electromagnetic nano-coatings [6-11]. Unitary nanofluids feature a single nanoparticle (metallic or carbon-based) suspended in a base fluid. Hybrid nanofluids feature two or more nanoparticles in the same base fluid. Furthermore, many novel electromagnetic nano-coatings are also strongly non-Newtonian i. e. they exhibit shear stress-strain characteristics which depart from the classical Newtonian viscous model. Their rheological characteristics make them particularly suitable for coating applications in extreme environments and examples include anti-microbial nano-coatings [12, 13], titania-based nano-epoxy resin coatings [14], nanosilica-based coatings [15], magnetic nano-fiber sensor coatings [16] and cobalt-based carbon nanotube electromagnetic coatings [17]. The robust simulation of coating flows with these intelligent materials requires a combination of electro-osmotics, magnetohydrodynamics, nanofluid dynamics and also non-Newtonian behaviour. This has motivated researchers to develop multi-physical boundary layer coating flow models in recent years. Many different non-Newtonian models have been utilized to study coating flows of wedge bodies including the Reiner-Rivlin second grade model [18], power-law model [19], Eyring-Powell model [20] and Eringen micropolar model [21], An alternative model which is suitable also for smart coatings is the tangent hyperbolic model which is a rate type non-Newtonian model, is known to be valid for both low and high shear rates and includes both relaxation time and the retardation time characteristics. Many investigators have used the tangent hyperbolic model in recent years for both nanofluids and conventional fluids. Malik et al. [22] deployed the tangent hyperbolic model to study hydromagnetic coating flow on an elongating cylindrical body with a finite difference method. Kumar et al. [23] studied two-phase magnetized radiative tangent hyperbolic fluid flow from a stretching surface. Tangent hyperbolic nanofluid flows were examined by Gharami *et al.* [24], Hayat *et al.* [25], Khan *et al.* [26] and Basha *et al.* [27], using different nanoscale models (Tiwari-Das volume fraction and Buongiorno two-component formulations). Prakash *et al.* [28] computed the combined effects of electrical and magnetic field on tangent hyperbolic radiative bioconvection nanofluid flow from a bi-directional stretching surface. Non-Newtonian nanofluid flows from a wedge configuration have also received some attention. Umavathi [29] studied the magnetized micropolar nanofluid flow from a wedge with Hall and ionslip current effects, considering both iron and copper nanoparticles and different base fluids. Ali *et al.* [30] used Oldroyd B and Jeffrey viscoelastic models to simulate the magnetic rheological flow from a shrinking/expanding wedge with activation energy effects. Ali et al. [31] used a finite element technique to compute the Carrea nanofluid magnetohydrodynamic boundary layer flow from a moving wedge, noting that the flow is decelerated with increasing unsteadiness parameter and wedge angle.

The above studies did not consider the collective effects of *non-Darcy porous media, combined electrical and magnetic field and the tangent hyperbolic nanofluid rheology for coating flow on a wedge geometry*. The novelty and focus of the present study is the consideration of zeta potential electro-osmotic effects and wall transpiration (suction/injection) which have not been addressed for such coatings previously. The present model therefore provides a more comprehensive examination of multiple effects on non-Newtonian electromagnetohydrodynamic coating flows and has not been communicated in the literature hitherto. A *Darcy-Forchheimer* model is adopted for non-Darcy effects following [32,33, 34]. The effect of zeta-potential is also included. The ternary composite nanofluid comprises three nanoparticles (Al_2O_3, TiO_2 and SiO_2) with aqueous base fluid (H_2O). The governing conservation partial differential equations for continuity and momentum and associated boundary conditions at the wedge surface and free stream are transformed with appropriate similarity variables. The emerging ordinary differential nonlinear boundary value problem is numerically solved in MATLAB. Validation with earlier studies is included. The effects of the Weissenberg number, zeta potential parameter, magnetic field parameter, electric field parameter, wall suction/injection parameter, porous medium permeability

(Darcy) parameter, Forchheimer parameter and electroosmosis parameter on fluid axial velocity, electric potential and skin friction coefficient distributions are visualized graphically and documented in tables. The model is applicable to smart coatings for a range of industrial applications including aerospace (wings), nuclear reactor wall, surface sensors and biomedical devices. The ternary hybrid non-Newtonian nanofluid afford a wider range of functionalities than existing coatings in this regard via improved viscosity, anti-corrosion characteristics, tuning under electrical and magnetic fields and enhanced durability under extreme loadings.

2. MATHEMATICAL FORMULATION

2.1 Definition of the problem

Consider the two-dimensional laminar incompressible non-Newtonian tangent hyperbolic ternary hybrid nanofluid boundary layer flow external to the surface of a permeable wedge that is embedded in a Darcy-Forchheimer porous medium. As shown in **Figure 1**, the Cartesian coordinate system (*x*, *y*) is selected in such a way that the origin is fixed at the apex of the wedge, the x-axis is directed along the surface of the wedge, and the y-axis is normal to the surface of the wedge. This is done so that the wedge can be represented by a triangle with its base at the apex. The flow is caused by the stretching of the wedge with a wall velocity of $U_w = \frac{bx^m}{1-ct}$,, and the external flow of the nanofluid has a free stream velocity of $U_e = \frac{ax^m}{1-ct}$. A static magnetic field $B = (0, B_0)$ acts in a direction that is normal to the surface of the wedge and an electrical field ϕ_x is applied parallel to the wedge surface. Here, t is the variable that represents time, the parameter constants are a, b, *m* and *c* in which $b < 0$ and $b > 0$ denote the rate of shrinking or stretching of the wedge. The constraint that the wedge angle should be aligned is called the Falkner–Skan power-law constraint (m). The gradient of the Hartree pressure factor is denoted by $\beta = \frac{2m}{1+m}$, and it corresponds to $\beta = \frac{\Omega}{\pi}$ for the entire wedge angle.

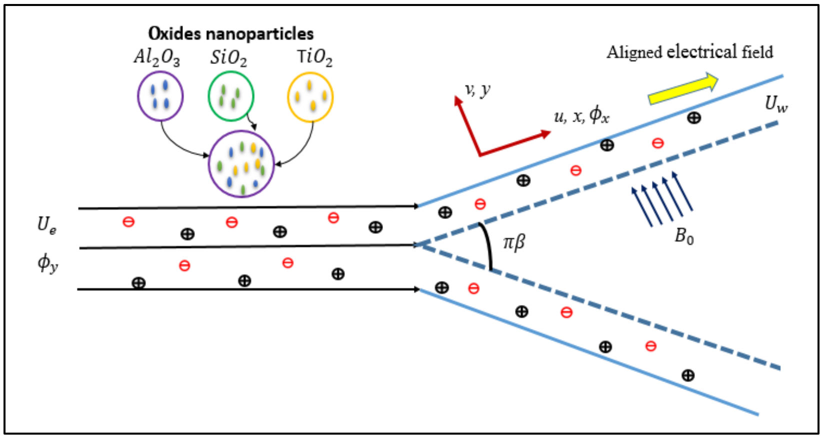

Fig. 1 Electromagnetic tangent hyperbolic nanofluid boundary layer coating flow on a wedge

The Falkner-Skan boundary layer formulation is a simplified mathematical model used to describe the flow of a fluid past a wedge-shaped obstacle. It is often used as a benchmark problem to test and validate computational fluid dynamics codes. However, there is some uncertainty associated with the wedge flow model and its assumptions, which can have implications for describing physical phenomena.

- **Assumptions about the properties of the fluid:** The wedge flow model assumes that the fluid is both incompressible and inviscid, which means it doesn't have any frictional forces and its density doesn't change. While these assumptions are appropriate for some applications, such as low-speed flows, they may not be valid for high-speed flows or flows with complex geometries. Ignoring buoyancy effects
- **Two-dimensional flow assumption:** The wedge flow model is typically formulated in two dimensions, assuming that the flow is uniform in the third dimension. This assumption may not be valid for flows with significant three-dimensional effects, such as vortex shedding or secondary flow patterns.
- **Simplified geometry:** The wedge flow model assumes a simple geometry, namely a wedge-shaped obstacle in a uniform flow.
- **Uncertainty in experimental data:** The wedge flow model is often used as a benchmark problem for CFD validation, but there is uncertainty associated with the experimental data used to validate the model.

2.1 Governing equations of the problem

For tangent hyperbolic liquid, the rheological constitutive equations are [31]:

$$S = -PI + \tau, \tag{1}$$

$$\tau = -[\mu_\infty + (\mu_0 + \mu_\infty)\tanh(\Gamma\dot{\gamma})^n]\dot{\gamma}, \tag{2}$$

where $-PI$ denotes the spherical component of the stress resulting from the incompressibility restriction, the additional stress tensor is denoted by τ, μ_∞ denotes the viscosity at an infinite shear rate, μ_0 denotes the viscosity at a zero-shear rate viscosity, Γ denotes the constant time, n denotes the power law index parameter and $\dot{\gamma}$ is shear rate which is characterized as:

$$\dot{\gamma} = \sqrt{\frac{1}{2}\sum_i \sum_j \dot{\gamma}_{\mathrm{ij}}\dot{\gamma}_{\mathrm{ji}}} = \sqrt{\frac{1}{2}\Pi}, \tag{3}$$

$$\Pi = \frac{1}{2}\, trac\left(grad(V) + \left(grad(V)\right)^T\right)^2$$

where Π denotes the invariant of second strain tensor. For the case of $\mu_\infty = 0$, $\Gamma\dot{\gamma} < 1$.
The component of the additional stress tensor may be represented as follows:

$$\tau = -\mu_0|(\Gamma\dot{\gamma})^n|\,\dot{\gamma} = -\mu\left|\left(1 + (\Gamma\dot{\gamma} - 1)\right)^n\right|\dot{\gamma} = -\mu_0|1 + n(\Gamma\dot{\gamma} - 1)|\dot{\gamma}. \tag{4}$$

The Cartesian form of governing equations (mass and momentum conservation) for boundary layer flow of an incompressible, hyperbolic tangent nanofluid under the dual effect of electric and magnetic fields from a porous wedge to a Darcy-Forchheimer permeable medium are given by [31-33]:

$$\frac{\partial u}{\partial x} + \frac{\partial v}{\partial y} = 0, \tag{5}$$

$$\frac{\partial u}{\partial t} + u\frac{\partial u}{\partial x} + v\frac{\partial u}{\partial y} = -\frac{1}{\rho_{THNF}}\frac{\partial P}{\partial x} + \nu_{THNF}\left[(1-n) + \sqrt{2}\, n\Gamma\,\frac{\partial u}{\partial y}\right]\frac{\partial^2 u}{\partial y^2} - \left(\frac{\sigma_{THNF}B_0^2}{\rho_{THNF}} + \frac{\nu_{THNF}}{K}\right)u - Fu^2 + \frac{\rho_e\phi_x}{\rho_{THNF}}, \tag{6}$$

Here u and v are x and y components of velocity respectively, P is the pressure, kinematic viscosity of THNF (ternary hybrid nanofluid) is ν_{THNF}, THNF density is ρ_{THNF}, THNF dynamic viscosity is μ_{THNF}, THNF electrical net charge thickness ρ_e ,F is the Forchheimer resistance factor (non-Darcy inertial drag coefficient) which is defined as $F = \frac{C_b}{\sqrt{K}}$, where $C_b$is the drag force and

K is the permeability of the porous medium. Since the pressure is independent of the direction that is perpendicular to the boundary layer, it is possible to determine the pressure by using the inviscid flow that is located outside of the boundary layer. The free stream (boundary layer edge) velocity of the tangent hyperbolic nanofluid $U_e(x,t)=\frac{ax^m}{1-ct}$ is assumed in Eq. (6). When $u=U_e$, $v=0$ and $\phi_x=\phi_y$ are taken into account outside of the boundary layer, the x-momentum equation may be written as:

$$-\frac{1}{\rho_{THNF}}\frac{\partial P}{\partial x}=\frac{\partial U_e}{\partial t}+U_e\frac{\partial U_e}{\partial x}+\left(\frac{\sigma_{THNF}B_0^2}{\rho_{THNF}}+\frac{\nu_{THNF}}{K}\right)U_e+FU_e^2-\frac{\rho_e\phi_y}{\rho_{THNF}}, \qquad (7)$$

Substituting Eq. (7) into Eq. (6), the latter may be rewritten as follows:

$$\frac{\partial u}{\partial t}+u\frac{\partial u}{\partial x}+v\frac{\partial u}{\partial y}=\frac{\partial U_e}{\partial t}+U_e\frac{\partial U_e}{\partial x}+\nu_{THNF}\left[(1-n)+\sqrt{2}\,n\Gamma\,\frac{\partial u}{\partial y}\right]\frac{\partial^2 u}{\partial y^2}-\left(\frac{\sigma_{THNF}B_0^2}{\rho_{THNF}}+\frac{\nu_{THNF}}{K}\right)(u-U_e)-F(u^2-U_e^2)+\frac{\rho_e(\phi_x-\phi_y)}{\rho_{THNF}}, \qquad (8)$$

2.3 Thermophysical properties of ternary hybrid nanofluid (THNF):

The *density* of THNF is given by the following expression, following [35-38]:

$$\rho_{THNF}=\phi_1\rho_1+\phi_2\rho_2+\phi_3\rho_3+(1-\phi_1-\phi_2-\phi_3)\rho_f, \qquad (9)$$

Here ρ_1,ρ_2,ρ_3 are the densities of the first, second and third nanoparticle, ϕ_1,ϕ_2,ϕ_3 are the volume fractions of first, second and third nanoparticles respectively and ρ_f is the density of base fluid (water).

The *dynamic viscosity* of ternary hybrid nanofluid is taken as [35-38]:

$$\mu_{hnf}=\left(\mu_{nf,1}\phi_1+\mu_{nf,2}\phi_2+\mu_{nf,3}\phi_3\right)/\phi \qquad (10)$$

Where $\mu_{nf,i}=\mu_f\left(1+B_i\phi+C_i\phi^2\right)$ (11)

Here the following notations apply: $\mu_{nf,i}$ is the dynamic viscosity of ith type nanoparticle (with given shape) suspension, μ_f is the dynamic viscosity of base fluid, B,C are the viscosity enhancement coefficients.

Electrical conductivity of ternary hybrid nanofluid may be characterised as:

$$\frac{\sigma_{thnf}}{\sigma_{hnf}} = \frac{(1+2\phi_1)\sigma_1+(1-2\phi_1)\sigma_{hnf}}{(1-\phi_1)\sigma_1+(1+\phi_1)\sigma_{hnf}}, \tag{12}$$

where $\frac{\sigma_{hnf}}{\sigma_{nf}} = \frac{(1+2\phi_2)\sigma_2+(1-2\phi_2)\sigma_{nf}}{(1-\phi_2)\sigma_2+(1+\phi_2)\sigma_{nf}}$ and $\frac{\sigma_{nf}}{\sigma_f} = \frac{(1+2\phi_3)\sigma_3+(1-2\phi_3)\sigma_f}{(1-\phi_3)\sigma_3+(1+\phi_3)\sigma_f}$.

Here $\sigma_1, \sigma_2, \sigma_3$ are the electrical conductivites of first nanoparticle, second nanoparticle and third nanoparticle, respectively; and σ_f is the base electrical conductivity. Table 1 gives shape factors for different nanoparticle geometries and Table 2 provides the thermo-physical constants of the nanoparticles as well as the base fluid, respectively.

Table 1 Parameters for defining shape and properties of nanoparticles [45]

Shape of nanoparticles	B	C
Platelets	37.1	612.6
Cylindrical	13.5	704.4
Spherical	2.5	6.2

Table 2 Thermophysical properties of oxides nanoparticles [35-38]

Oxides	H_2O	Al_2O_3	TiO_2	SiO_2
Density $(Kg\, m^{-3})$	997.1	3970	4250	3970
Electric conductivity (Sm^{-1})	5.5×10^{-6}	35×10^{6}	3.5×10^{6}	10^{-23}

2.4 Electrical potential

The electrical field generates an electrical double layer via electro-osmotic body force effects. The electrical potential distribution in the electrical double layer is analyzed using the Boltzmann-Poisson equation (EDL):

$$div\boldsymbol{D} = \rho_e, \tag{13}$$

Here $\boldsymbol{D}(=\epsilon_{ef}\overline{\Phi})$ which is the rate of volumetric change, and $\bar{\rho}_e$ and ϵ_{ef} are respectively the density and the permittivity of the dielectric magnetic nanofluid. Then:

$$div\left(-\epsilon_{ef}\; grad\; \overline{\Phi}\right) = \rho_e, \tag{14}$$

At every point on the permeable wedge surface, the permittivity is the same. The appropriate equation for electrical potential is:

$$\nabla^2\bar{\Phi} = -\frac{\rho_e}{\epsilon_{ef}}, \qquad (15)$$

and

$$\rho_e = \bar{e}\bar{z}_1(n^+ - n^-), \qquad (16)$$

Here the numbers n^+ and n^- represent the anticipated cation and anion densities at a concentration of n_0, respectively.

Assuming no EDL overlap, the Boltzmann distribution may be written as:

$$n^{\pm} = n_0 \exp\left(\pm\frac{\bar{e}\bar{z}_1\bar{\Phi}}{K_B T_w}\right), \qquad (17)$$

Here the electronic charge and charge balance are represented, respectively, by $\bar{e}$ and $\bar{z}_1$, Boltzmann constant is denoted by K_B and T_w is the average electrolytic solution temperature.

To apply Eqn. (17), the values of the ion counts are replaced in Eqn. (16), leading to:

$$\rho_e = -2\bar{z}_1\,\bar{e}\,n_0 \sinh\left(\frac{\bar{z}_1\bar{e}\,\bar{\Phi}}{K_B T_w}\right), \qquad (18)$$

The Boltzmann-Poisson equation Eqn. (15) is modified by invoking the second order differential equation for charge density i. e. Eqn. (18) to obtain the electrical potential distribution:

$$\frac{\partial\bar{\Phi}}{\partial x^2} + \frac{\partial^2\bar{\Phi}}{\partial y^2} = -2\bar{z}_1\,\bar{e}\,n_0 \sinh\left(\frac{\bar{z}_1\bar{e}\,\bar{\Phi}}{K_B T_w}\right). \qquad (19)$$

2.5 Dimensional boundary conditions

The relevant boundary conditions at the wedge surface (wall) and free stream are defined as follows [18-20]:

$$u = U_w(x) = -\gamma\, U_e(x),\ v = V_w\,, \bar{\phi} = \bar{\xi} \quad at\ \ y = 0, \qquad (20)$$

$$u = U_e(x),\ \ \bar{\phi} \to 0 \qquad as\ \ y \to \infty. \qquad (21)$$

Here γ defines the moving wedge parameter. Three cases of are of pertinence for materials processing coating operations [39]: $\gamma > 0$ corresponds to a contracting wedge, $\gamma < 0$ indicates a stretching wedge, $\gamma = 0$ denoted as a stationary wedge.

2.6 Scaling analysis

Taking into consideration the stream function $\psi(x, y)$ in such a way that $u = \frac{\partial\psi}{\partial y}; v = -\frac{\partial\psi}{\partial x}$ and then introducing the following similarity transformations [34]:

$$U_e = \frac{ax^m}{1-ct}, U_w = \frac{bx^m}{1-ct}, V_w = \frac{v_0}{\sqrt{1-ct}}, \psi = \frac{\sqrt{2\nu_f x U_e}}{\sqrt{1+m}}\, f, \eta = y\frac{\sqrt{(1+m)U_e}}{\sqrt{2\nu_f x}}, \phi = \frac{\bar{z}_1 \bar{e}\, \bar{\Phi}}{K_B T_w}, \tag{22}$$

Utilizing these transformations, Eqn. (5) is automatically satisfied, and Eqns. (8) and (19) are converted to:

$$A_\nu f'''\left((1+n) + nWe\sqrt{1+m}\, f''\right) + \frac{A}{1+m}(2 - f''\eta - 2f') + \beta(1 - f'^2) + ff'' - \frac{(A_\sigma M^2 + A_\nu\, A_\rho Da)\,(f'-1)}{A_\rho(1+m)} + Fr(f'^2 - 1) + \frac{U_E}{A_\rho}(1+m)\phi'' = 0, \tag{23}$$

$$(1+m)\phi'' = \kappa^2 \sinh(\phi), \tag{24}$$

The transformed dimensionless boundary conditions (20, 21) emerge as:

$$f' = -\gamma,\ f = \frac{S}{1+m}, \phi = \xi \quad at \ \ \eta = 0, \tag{25}$$

$$f' = 1,\ \ \phi \to 0 \qquad as \ \ \eta \to \infty. \tag{26}$$

Here $A = \frac{c}{ax^{m-1}}$ is the unsteadiness parameter, $M^2 = \frac{2\sigma_f B_0^2 x}{U_e \rho_f}$ is the magnetic parameter, $Da = \frac{2x\nu_f}{KU_e}$ is the Darcy permeability parameter, $We = \frac{\Gamma\, U_e^{\frac{3}{2}}}{\sqrt{\nu_f x}}$ is the Weissenberg number, Fr is Forchheimer number $(= 2xF)$, $U_E = \frac{U_{HS}}{U_e}$ is the electric field parameter in which Helmholtz-Smoluchowski velocity is $U_{HS} = \frac{-K_B T_w \epsilon_{ef}(\phi_x - \phi_y)}{\mu_f \bar{z} e}$, $\kappa = \frac{m_1^2 \nu_f x}{U_e}$ is electroosmosis parameter (where Debye-Hückel parameter is $m_1^2 = \frac{4\bar{z}^2 e^2 n_0}{\epsilon_{ef} K_B T_v}$) , $S = -\frac{v_0\sqrt{2x}}{\sqrt{\nu_f u_e(1-ct)}}$ is the wedge surface suction/injection parameter (for suction ($S < 0$) and for blowing i.e. injection ($S > 0$)) and zeta potential parameter is $\xi = \frac{\tilde{z}e\tilde{\xi}}{K_B T_v}$.

3. WALL CHARACTERISTIC PHYSICAL QUANTITIES

The skin friction coefficient is a key variable of importance in coating flows and is also known as the surface shear stress (wall velocity gradient). It may be defined as:

$$C_f = \frac{\tau_w}{\rho_{THNF} U_e^2}, \tag{27}$$

where $\tau_w = \mu_{THNF} \left[(1-n)\frac{\partial u}{\partial y} + \frac{n\Gamma}{\sqrt{2}} \left(\frac{\partial u}{\partial y}\right)^2 \right]_{y=0}$,

Via the similarity transformations (22), the required dimensionless skin friction expression takes the form:

$$\sqrt{Re}\, C_f = A_\nu \left[\sqrt{1+m}\,(1-n) + \frac{(1+m)}{2}\, n\, We\, f''(0) \right] f''(0)\,, \tag{28}$$

Where $Re = \frac{U_e x}{\nu_f}$ is a local Reynolds number.

In Eqns. (23) and (28), the following constants are used:

$$A_\rho = \frac{\phi_1\rho_1 + \phi_2\rho_2 + \phi_3\rho_3}{\rho_f} + (1 - \phi_1 - \phi_2 - \phi_3),$$

$$A_\mu = ((1 + B_1\phi + C_1\phi^2)\phi_1 + (1 + B_2\phi + C_2\phi^2)\phi_2 + (1 + B_3\phi + C_3\phi^2)\phi_3)/\phi,\ A_\nu = \frac{A_\mu}{A_\rho},$$

$$A_\sigma = A_{hnf} \frac{(1+2\phi_1)\sigma_1 + (1-2\phi_1)A_{hnf}}{(1-\phi_1)\sigma_1 + (1+\phi_1)A_{hnf}},$$

$$A_{hnf} = \left(\frac{(1+2\phi_3)\sigma_3 + (1-2\phi_3)A_f}{(1-\phi_3)\sigma_3 + (1+\phi_3)A_f}\right) \frac{\left((1+2\phi_2)\sigma_2 + (1-2\phi_2)\left(\frac{(1+2\phi_3)\sigma_3 + (1-2\phi_3)A_f}{(1-\phi_3)\sigma_3 + (1+\phi_3)A_f}\right)\right)}{\left((1-\phi_2)\sigma_2 + (1+\phi_2)\left(\frac{(1+2\phi_3)\sigma_3 + (1-2\phi_3)A_f}{(1-\phi_3)\sigma_3 + (1+\phi_3)A_f}\right)\right)}. \tag{29}$$

4. NUMERICAL SOLUTION AND VALIDATION

The strong nonlinearity arising in Eqn. (23) which is coupled to Eqn. (24) require a numerical solution. The highly accurate and stable bvp4c shooting method in MATLAB is therefore adopted. The Bvp4c formula is basically a Lobattao - IIIa collocation technique [40, 41]. With suitable substitutions, the higher-order differential Eqns. (23) and (24) may be reduced into first-order ordinary differential equations, as follows:

$$f = y(1); f' = y(2); f'' = y(3); f''' = y'(3); \phi = y(4); \phi' = y(5); \phi'' = y'(5), \tag{30}$$

where

$$y'(3) = \left(-\frac{A}{1+m}\left(2 - y(3)\eta - 2y(2)\right) - \beta(1 - y(2)^2) - y(1)y(3) + \frac{(A_\sigma M^2 + A_\nu A_\rho Da)\,(y(2)-1)}{A_\rho(1+m)} - \frac{U_E}{A_\rho}(1+m)y'(5)\right) / A_\nu\left((1+n) + nWe\sqrt{1+m}\,y(3)\right), \tag{31}$$

$$y'(5) = \frac{\kappa^2 \sinh(y(4))}{(1+m)}, \tag{32}$$

The associated boundary conditions take the form:

$$y(2) = -\gamma, y(1) = \frac{S}{1+m}, y(4) = \xi \quad at \;\; \eta = 0, \tag{33}$$

$$y(2) = 1, \;\; y(4) \to 0 \qquad as \;\; \eta \to \infty. \tag{34}$$

The mesh selection and error function are revitalized by the presence of a continuous solution. The disparity stays the same, with a magnitude of10^{-9}. At the value of $\eta = 8$, all numerical solutions converge asymptotically.

Using the finite difference algorithm bvp4c, the three-stage LobattoIIIa formula can be implemented [46, 47]. This is an illustration of a collocation formula, and the answer provided by the collocation polynomial is exact to the fourth degree at every point on the interval of integration and is C^1-continuous. The grid is chosen, and mistakes are handled based on the remainder of the continuous solution. This article findings are accurate to within 10^{-9} units. The problem-solving model contains 352 vertices. This issue was resolved with a grid size of 483, and a highest residual of 5.173×10^{-9}. After convergence is reached on a given mesh, the programmes make adjustments to the mesh in order to generate a solution with adequate precision using as few mesh points as practically possible. To validate the present numerical approach, comparison with previous simpler studies has been conducted. **Table 3** shows the present results for the velocity, $f'(\eta)$and skin friction , $f''(\eta)$, benchmarked against the earlier computations of Kandasamy *et al*.

[34] and White [42]. **Excellent correlation is achieved testifying to the accuracy of the present MATLAB bvp4c solutions.**

Table – 3: Comparison of present MATLAB solutions with [34, 42] for $f'(\eta)\ and\ f''(\eta)$.

$\boldsymbol{\eta}$	Kandasamy *et al.* [34]		White [42]		Present Solution	
	$\boldsymbol{f'(\eta)}$	$\boldsymbol{f''(\eta)}$	$\boldsymbol{f'(\eta)}$	$\boldsymbol{f''(\eta)}$	$\boldsymbol{f'(\eta)}$	$\boldsymbol{f''(\eta)}$
0.0	0	0.469686	0	0.469599	0	0.46969891643441
0.5	0.234267	0.465078	0.23423	0.46503	0.234276697704929	0.465127365137735
1.0	0.460628	0.434377	0.46063	0.43438	0.460627771046274	0.434463545861249
2.0	0.816687	0.255668	0.81669	0.25567	0.816685225121935	0.255691186224172
3.0	0.969046	0.067714	0.96905	0.06771	0.969049598861173	0.067698996031665
4.0	0.997773	0.006871	0.99777	0.00687	0.997772151844778	0.006870179538637

4.1 Stability analysis

The given problem is a boundary value problem that involves a system of six first order ordinary differential equations (ODEs) with five unknown functions $(\eta), y'(\eta), y'', y'''(\eta)$, $\phi(\eta), \phi'(\eta)\ and\ \phi''(\eta)$. The associated boundary conditions are given by equations (33) and (34) which is solved by using the shooting technique.

The stability and existence of the formulated problem can be analysed using the theory of nonlinear boundary value problems. A key tool for this analysis is the Sturm-Picone comparison theorem, which relates the eigenvalues of a linear boundary value problem to the stability and existence of a nonlinear boundary value problem.

To apply the Sturm-Picone comparison theorem, we need to linearize the given system of ODEs about the trivial solution $y(\eta) = y'(\eta) = y''(\eta) = y'''(\eta) = \phi(\eta) = \phi'(\eta) = \phi''(\eta) = 0$. We obtain the following linearized system:

$$y''''(\eta) = \phi''(\eta) = 0, \tag{35}$$

The boundary solution to the linearized system are the same as the boundary conditions for the original system, given by equations (33) and (34).

The general solution to the linearized system is given by:

$$y(\eta) = C_1 + C_2\eta + C_3\eta^2 + C_4\eta^3, \tag{36}$$

$$\phi(\eta) = C_5 + C_6\eta, \tag{37}$$

Where C_1, C_2, C_3, C_4, C_5 and C_6 are arbitrary constants. The boundary conditions (33) and (34) lead to the following equations for these constants.

$$C_1 = \frac{S}{1+m}, C_2 = \gamma, C_5 = \xi, C_3 = \frac{1-G}{6}, C_4 = -\frac{G}{6}, C_6 = 0, \tag{38}$$

where $G = A_V(1+n)/\big(A_\sigma M^2 + A_\nu A_\rho Da\big)(1+m)We\sqrt{1+m}$.

Using the Sturm-Picone comparison theorem, we can conclude that the nonlinear boundary value problem is stable and has a unique solution if and only if the linearized boundary value problem has only trivial solutions. The linearized boundary value problem has only trivial solution if and only if the boundary value problem:

$$y''''(\eta) + \lambda y(\eta) = 0, \tag{39}$$

With boundary conditions (33) and (34), has only trivial solutions. Here λ is an eigenvalue of the linearized boundary value problem.

The eigenvalues of the linearized boundary value problem are given by $\lambda_n = \left(\frac{n\pi}{L}\right)^4$, where L is a length scale determined by the problem parameters, and n is a positive integer.

Since the eigenvalues are all positive, the linearlized boundary value problem has only trivial solutions. Therefore, by the Sturm-Picone comparison theorem, the nonlinear boundary value problem is stable and has a unique solution.

5. RESULTS AND DISCUSSION

In this section, numerical solutions obtained for a wide range of control parameters are presented graphically for the electromagnetic nanofluid coating flow characteristics i.e. dimensionless velocity $f'(\eta)$, electric potential $\phi(\eta)$, and surface friction coefficient $f''(0)$. The computations consider three types of oxide nanoparticles i. e. Al_2O_3, TiO_2, SiO_2 with base fluid of water, H_2O. The nanoparticle value of Al_2O_3 is $\phi_1 = 0.03$, the nanoparticle value of TiO_2 is $\phi_2 = 0.02$ and the nanoparticle value of SiO_2 is $\phi_3 = 0.01$. The ternary hybrid nanofluid (THNF) is considered as Al_2O_3, TiO_2, SiO_2 with base fluid H_2O and the unitary nanofluid (UNF) is assumed to be Al_2O_3 with base fluid as water H_2O. Data has been extracted from appropriate references for the other parameters [3, 5, 22, 30, 44]. The selected ranges of parameters are suitable for real ternary nanocoating boundary layer flows. Results for dimensionless velocity distribution are discussed for various pertinent parameters for both cases of THNF and UNF in **Figs.2(a)-2(i)**.

Fig.2(a) shows the impact of the Darcy permeability parameter, *Da* on both THNF and UNF. Significantly greater velocity is computed with increment in Darcy number *Da* for both of the nanofluid cases. However, the UNF achieves larger magnitudes of velocity, both close to the wedge surface and further away from it. The increment in Darcy number corresponds to a boost in the permeability of the porous medium. The Darcian drag force is therefore depleted and less obstruction to the nanofluid is created by the porous medium solid fibers. Effectively the use of a single nanoparticle produces a thinner momentum boundary layer (greater flow acceleration) than a ternary nanofluid.

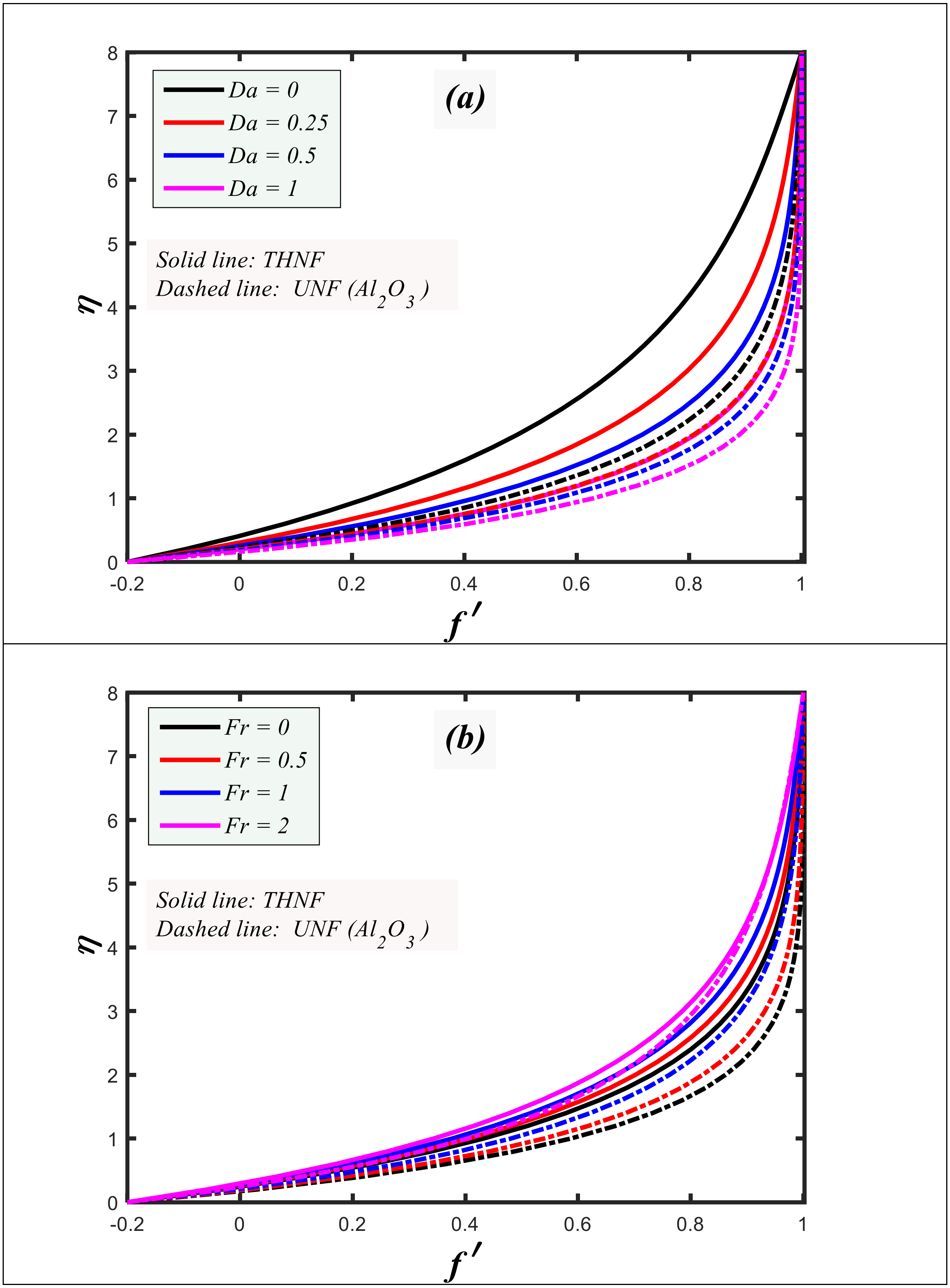
(a)
Da = 0
Da = 0.25
Da = 0.5
Da = 1
Solid line: THNF
Dashed line: UNF (Al_2O_3)
η
f'
0
1
2
3
4
5
6
7
8
-0.2
0
0.2
0.4
0.6
0.8
1
(b)
Fr = 0
Fr = 0.5
Fr = 1
Fr = 2
Solid line: THNF
Dashed line: UNF (Al_2O_3)
η
f'
0
1
2
3
4
5
6
7
8
-0.2
0
0.2
0.4
0.6
0.8
1

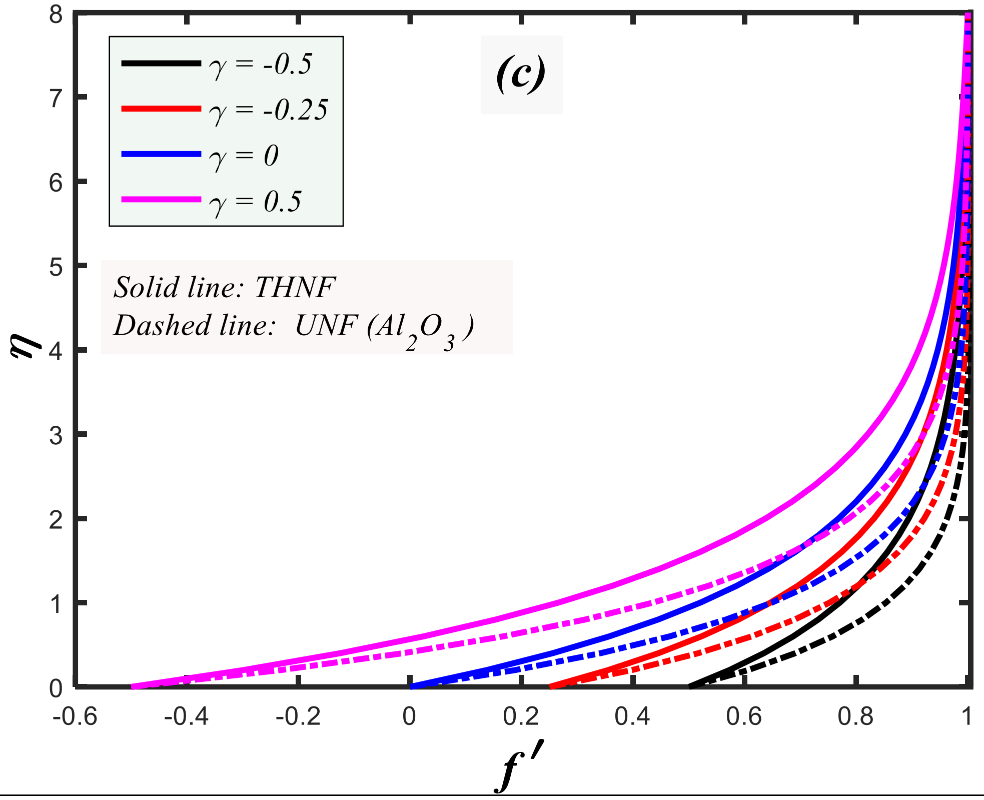
(c)
γ = -0.5
γ = -0.25
γ = 0
γ = 0.5
Solid line: THNF
Dashed line: UNF (Al2O3)
η
f′
0
1
2
3
4
5
6
7
8
-0.6
-0.4
-0.2
0
0.2
0.4
0.6
0.8
1

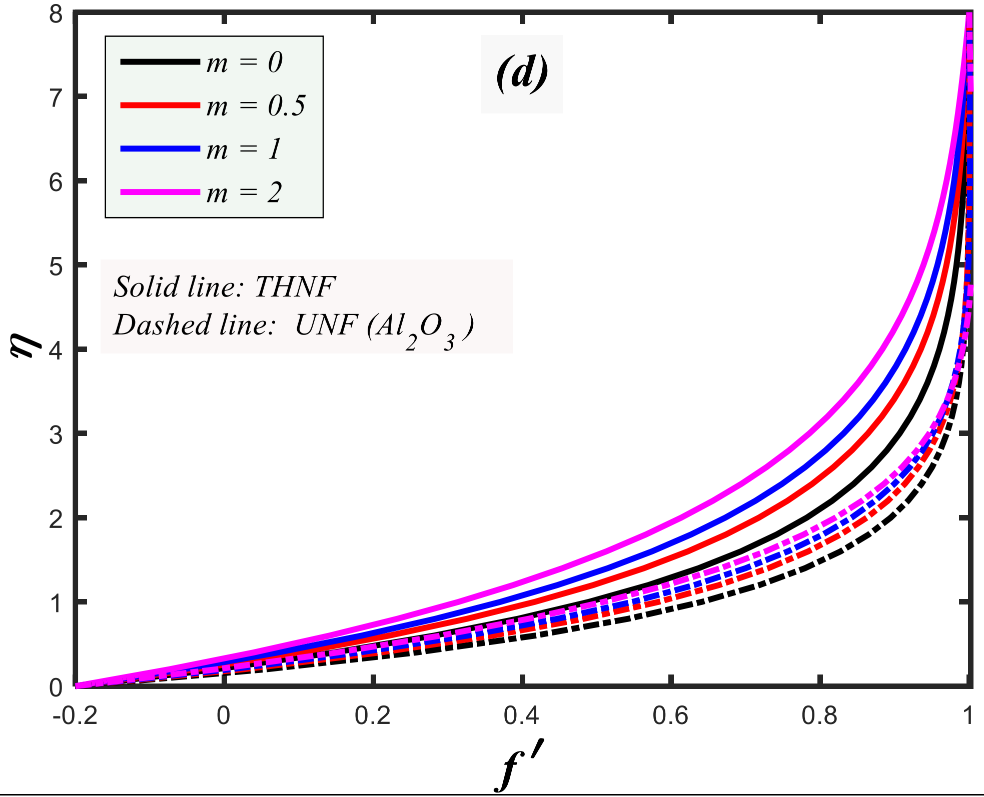
(d)
m = 0
m = 0.5
m = 1
m = 2
Solid line: THNF
Dashed line: UNF (Al2O3)
η
f′
0
1
2
3
4
5
6
7
8
-0.2
0
0.2
0.4
0.6
0.8
1

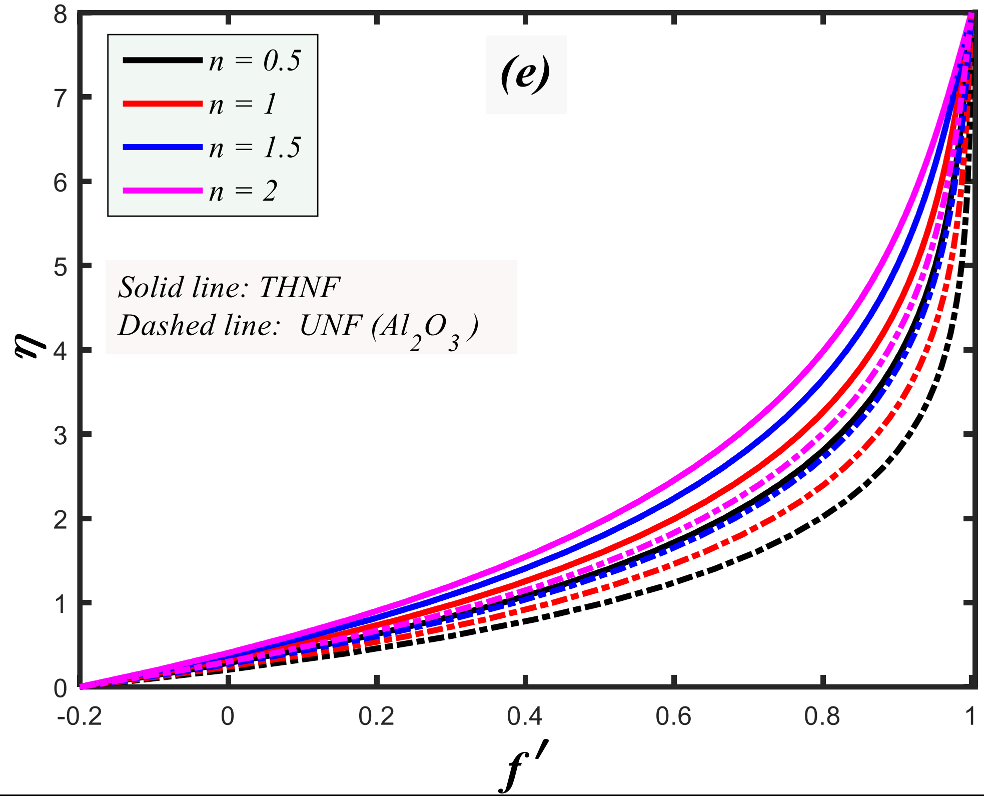
(e)
n = 0.5
n = 1
n = 1.5
n = 2
Solid line: THNF
Dashed line: UNF (Al2O3)
η
f′
0
1
2
3
4
5
6
7
8
-0.2
0
0.2
0.4
0.6
0.8
1

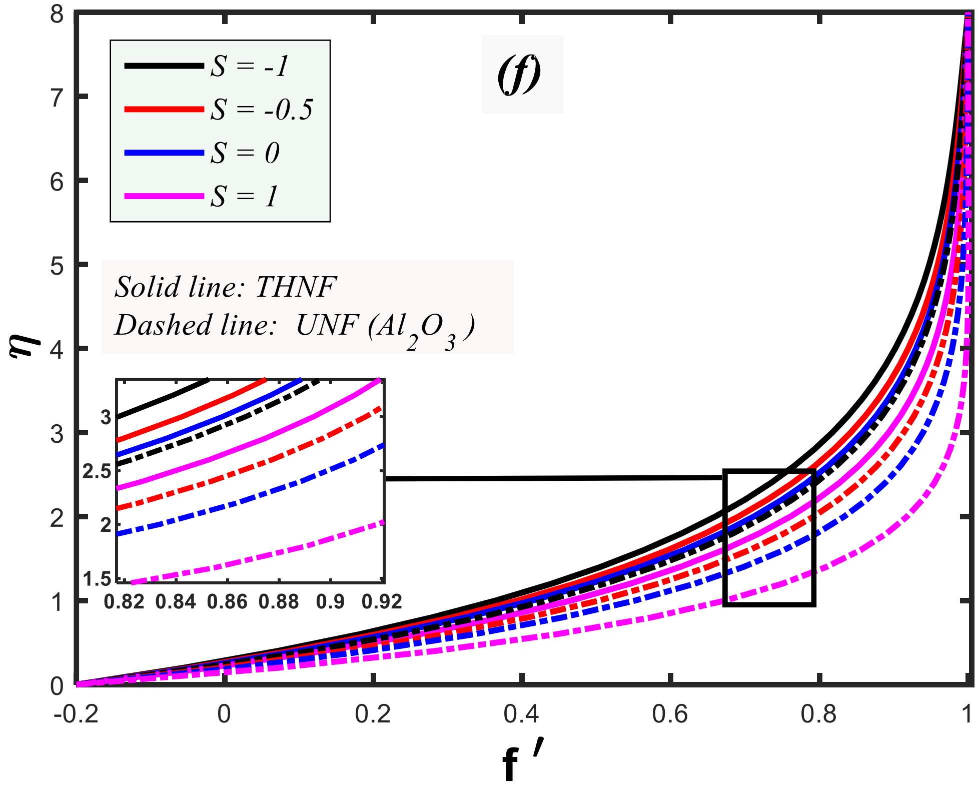
(f)
S = -1
S = -0.5
S = 0
S = 1
Solid line: THNF
Dashed line: UNF (Al2O3)
η
f′
0
1
2
3
4
5
6
7
8
-0.2
0
0.2
0.4
0.6
0.8
1
1.5
2
2.5
3
0.82
0.84
0.86
0.88
0.9
0.92

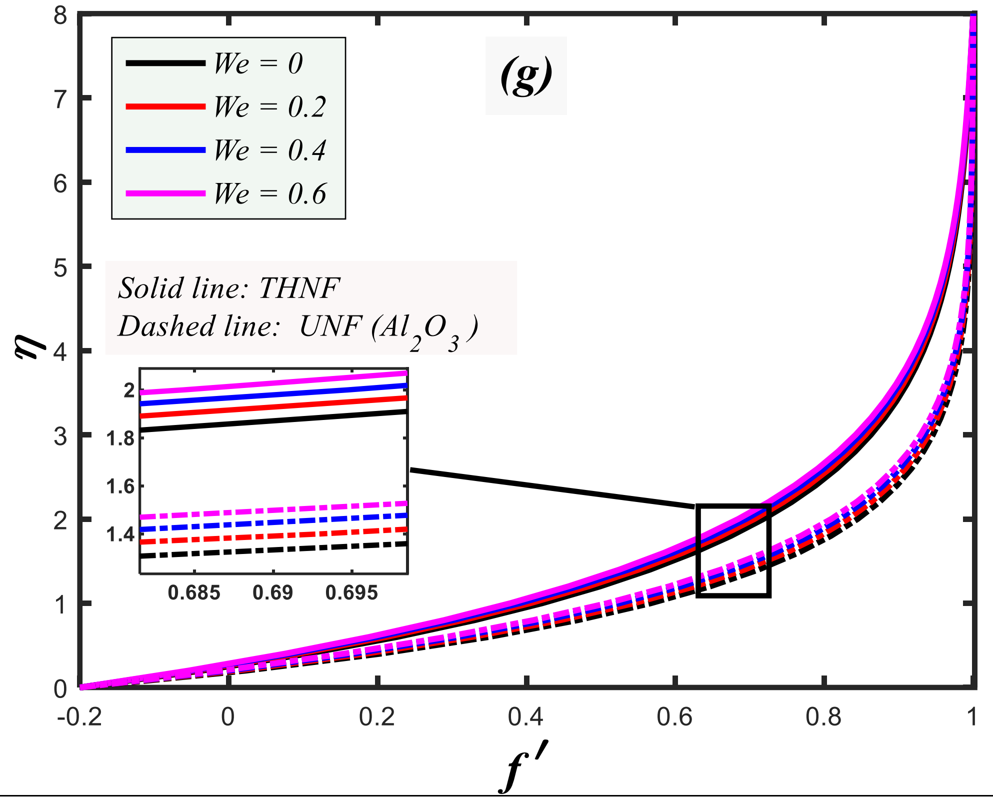
(g)
We = 0
We = 0.2
We = 0.4
We = 0.6
Solid line: THNF
Dashed line: UNF (Al_2O_3)
η
f′
-0.2
0
0.2
0.4
0.6
0.8
1
0
1
2
3
4
5
6
7
8
0.685
0.69
0.695
1.4
1.6
1.8
2

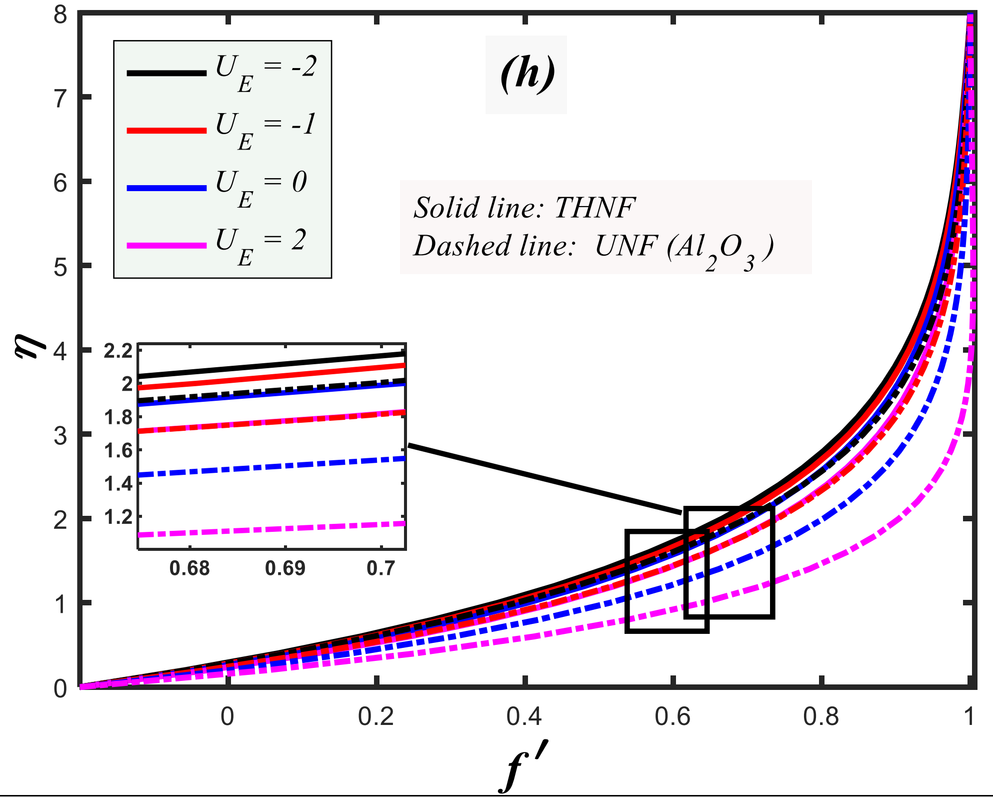
(h)
U_E = -2
U_E = -1
U_E = 0
U_E = 2
Solid line: THNF
Dashed line: UNF (Al_2O_3)
η
f′
0
0.2
0.4
0.6
0.8
1
0
1
2
3
4
5
6
7
8
0.68
0.69
0.7
1.2
1.4
1.6
1.8
2
2.2

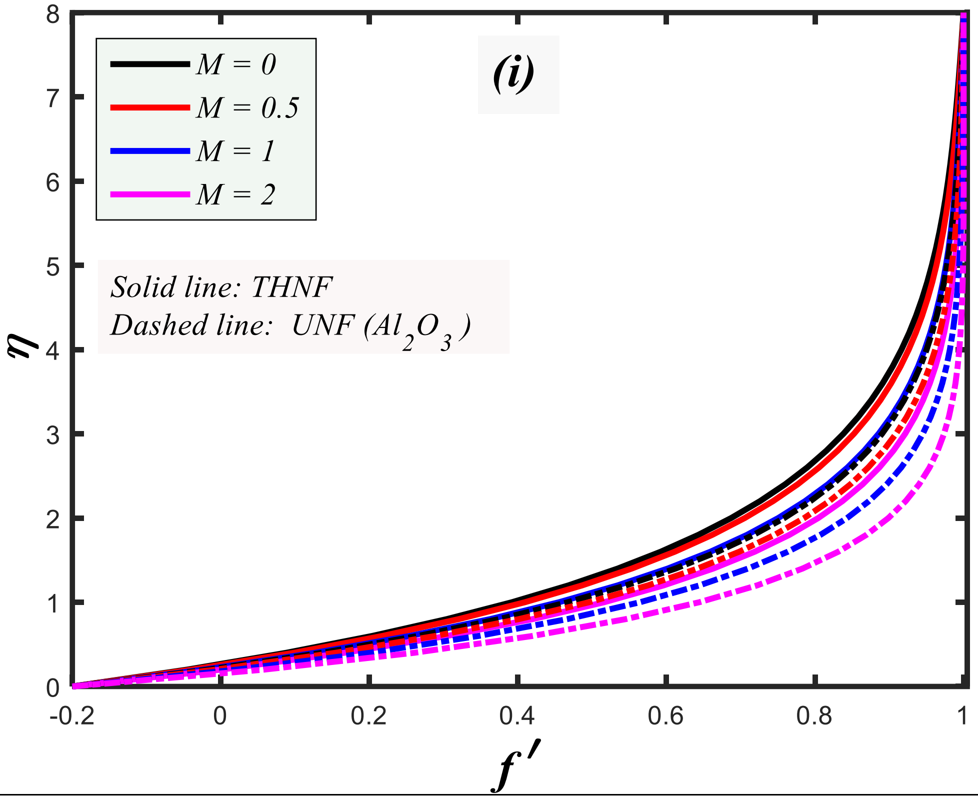

Figs. 2. Impacts of (a) Darcy number, (b) Forchheimer number, (c) moving wedge parameter, (d) Falkner-Skan power-law constant (wedge angle parameter), (e) rheological power-law index, (f) suction/injection parameter (g) Weissenberg number, (h) electric field parameter and (i) Hartmann number on axial velocity for fixed value of $\kappa = 1; m = 0.3; U_E = 2; n = 0.2; We = 0.1; Fr = 0.5; M = 2; Da = 0.5; A = 1; S = 0.5; \xi = 1, \gamma = 0.2, \phi_1 = 0.03; \phi_2 = 0.02; \phi_1 = 0.01$.

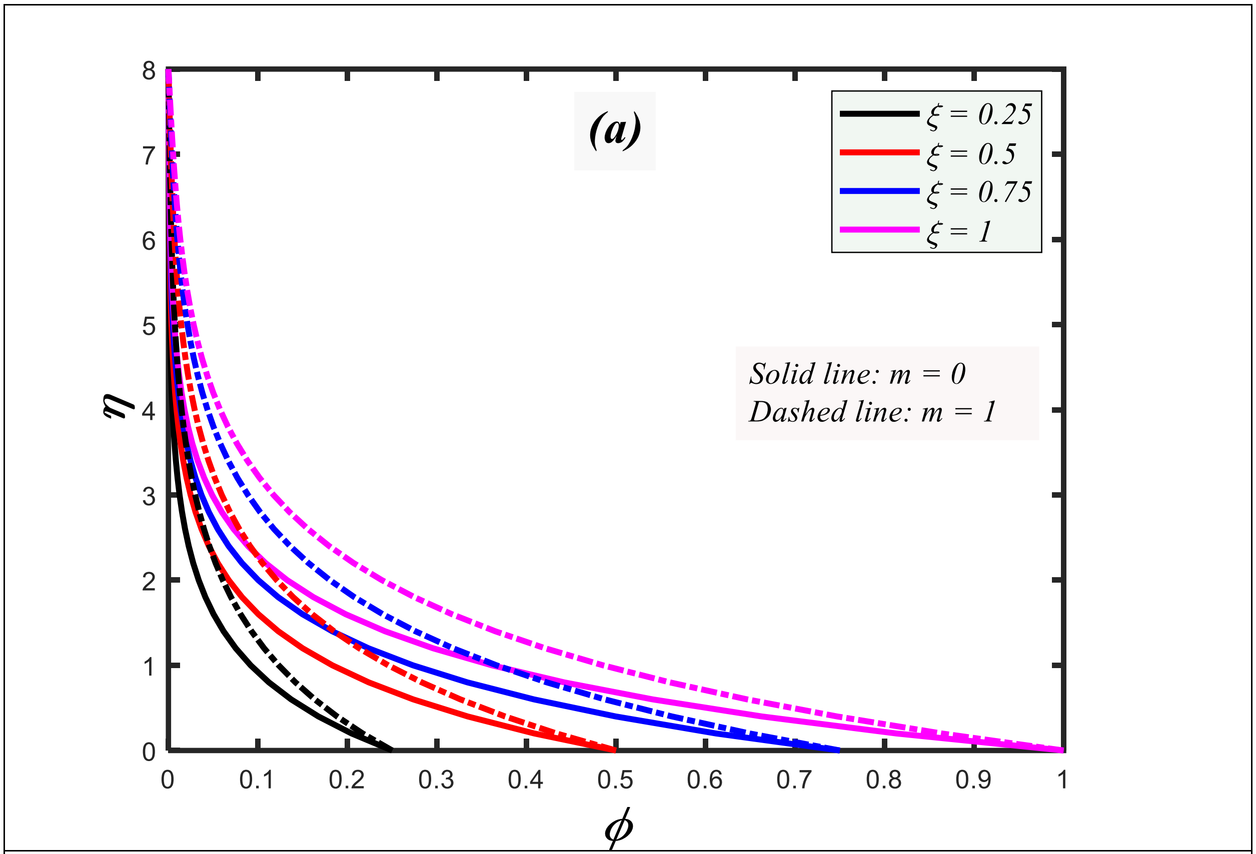
(a)
$\xi = 0.25$
$\xi = 0.5$
$\xi = 0.75$
$\xi = 1$
Solid line: m = 0
Dashed line: m = 1
η
0
1
2
3
4
5
6
7
8
ϕ
0
0.1
0.2
0.3
0.4
0.5
0.6
0.7
0.8
0.9
1

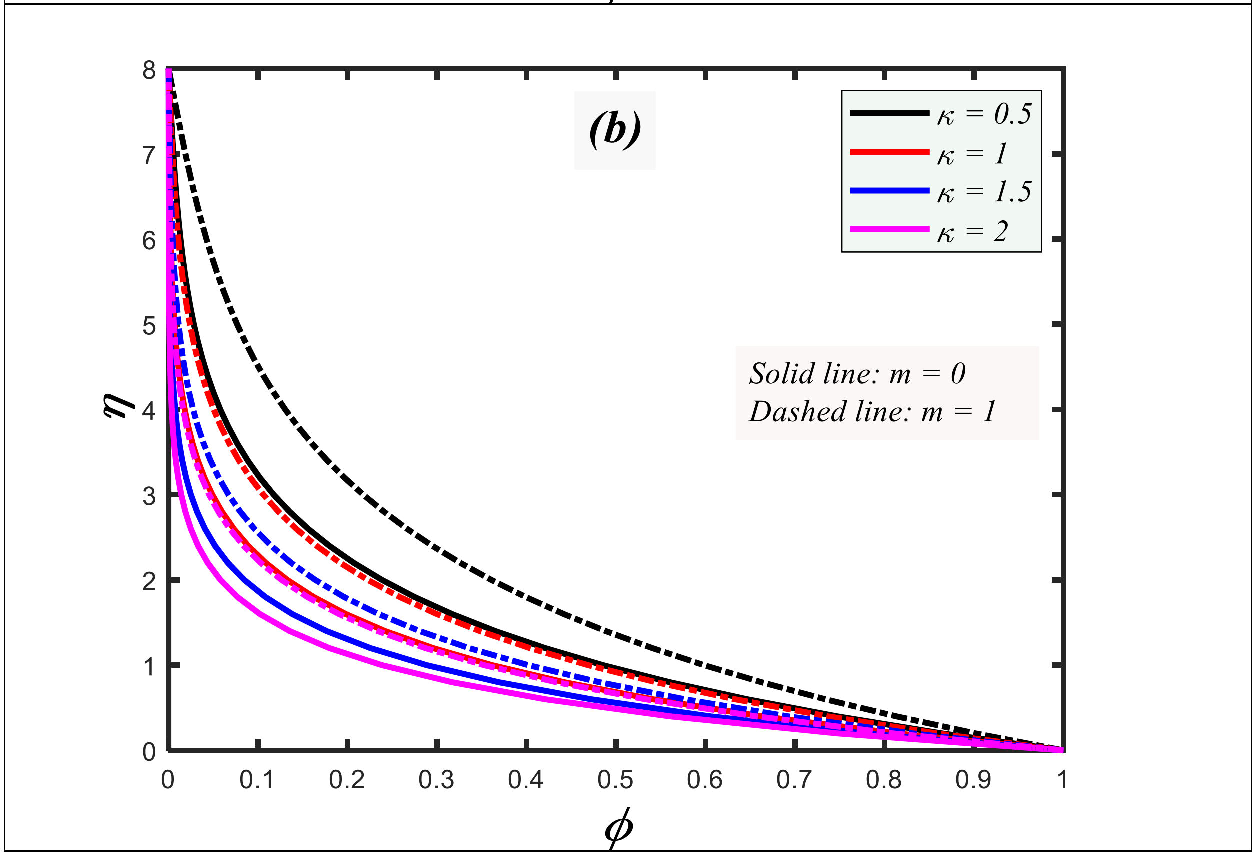
(b)
$\kappa = 0.5$
$\kappa = 1$
$\kappa = 1.5$
$\kappa = 2$
Solid line: m = 0
Dashed line: m = 1
η
0
1
2
3
4
5
6
7
8
ϕ
0
0.1
0.2
0.3
0.4
0.5
0.6
0.7
0.8
0.9
1

Figs. 3. Impacts of (a) zeta potential parameter and (b) electroosmosis parameter on electric potential profiles for fixed values of $\xi = 1$ and $\kappa = 1$.

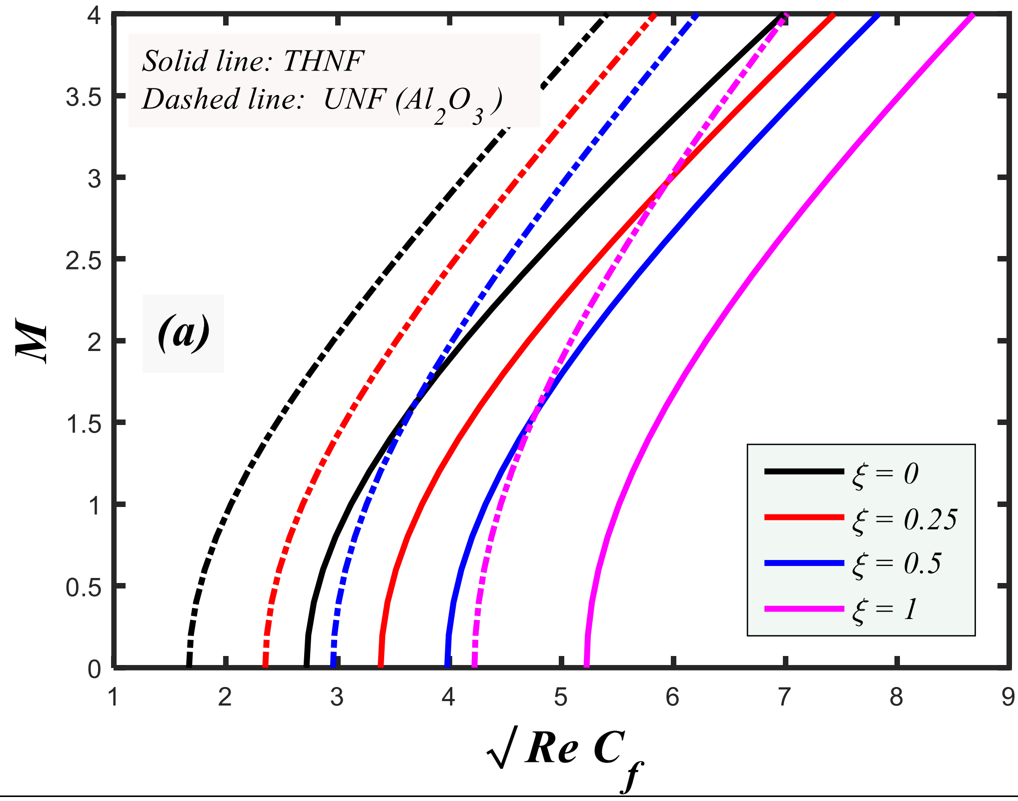

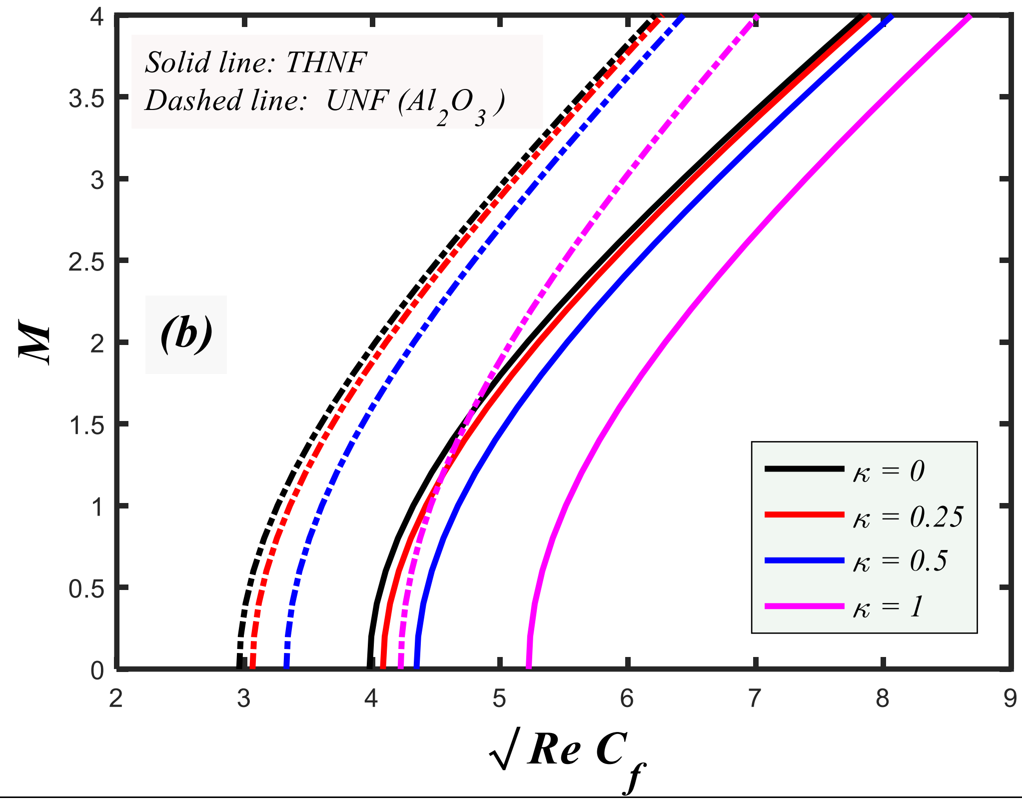
Solid line: THNF
Dashed line: UNF (Al_2O_3)
(b)
M
$\sqrt{Re}\,C_f$
κ = 0
κ = 0.25
κ = 0.5
κ = 1
0
0.5
1
1.5
2
2.5
3
3.5
4
2
3
4
5
6
7
8
9

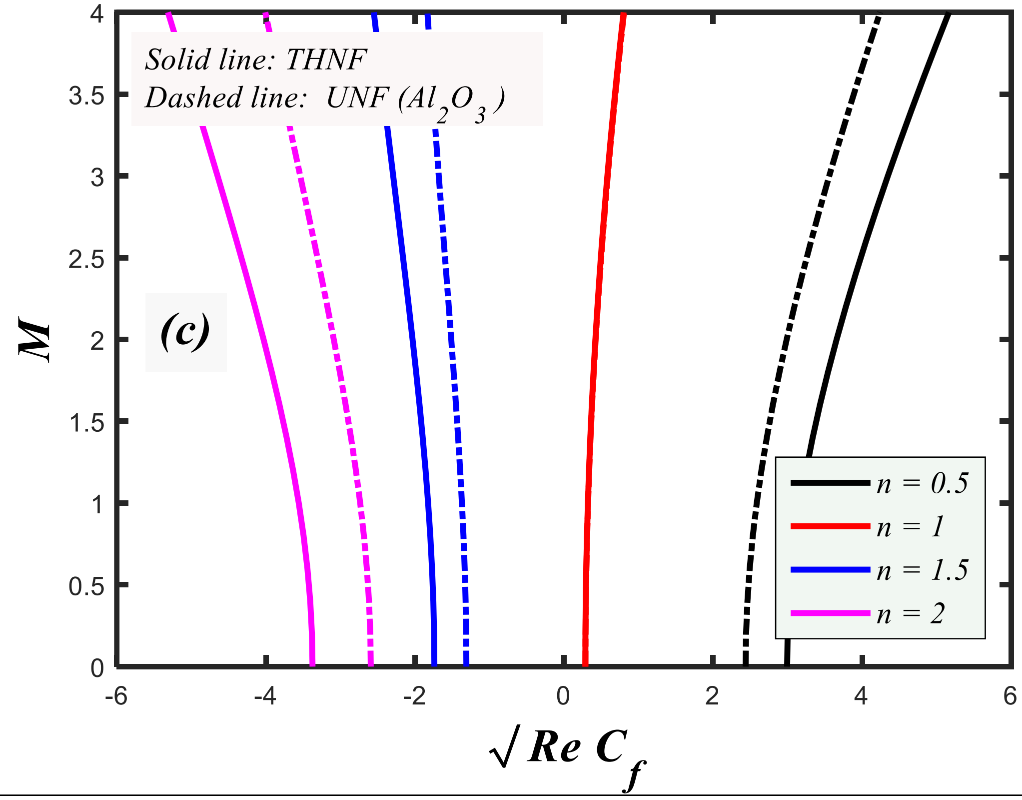
Solid line: THNF
Dashed line: UNF (Al_2O_3)
(c)
M
$\sqrt{Re}\,C_f$
n = 0.5
n = 1
n = 1.5
n = 2
0
0.5
1
1.5
2
2.5
3
3.5
4
-6
-4
-2
0
2
4
6

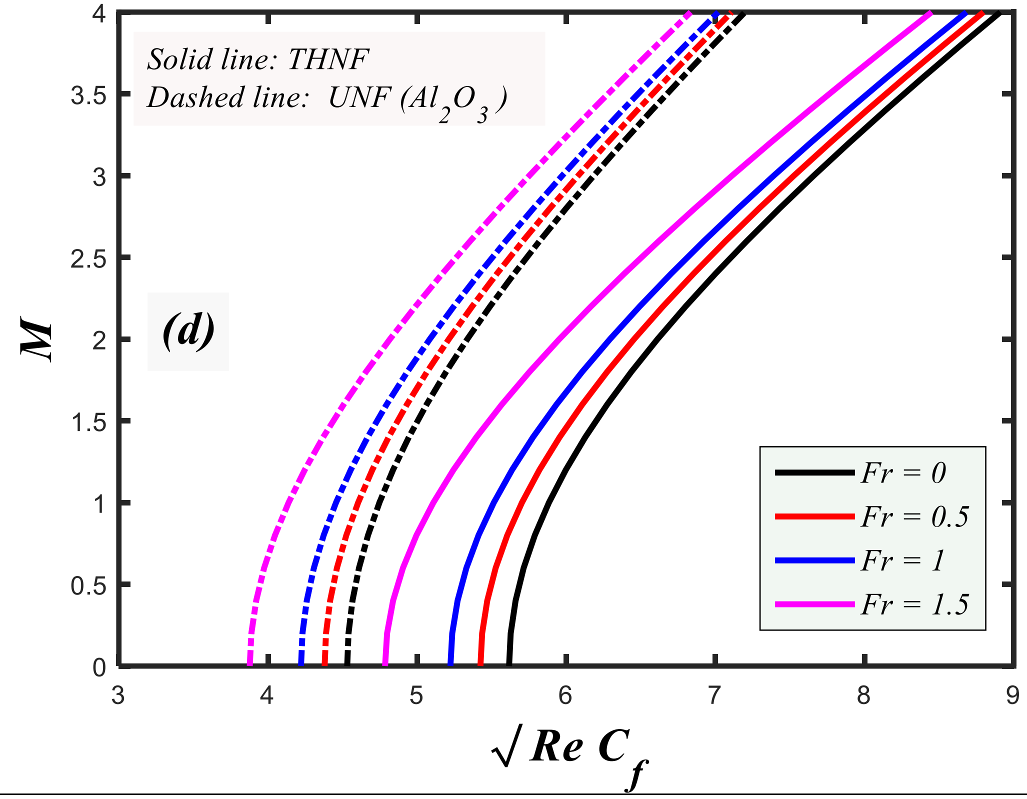
Solid line: THNF
Dashed line: UNF (Al_2O_3)
(d)
M
$\sqrt{Re}\, C_f$
Fr = 0
Fr = 0.5
Fr = 1
Fr = 1.5
0
0.5
1
1.5
2
2.5
3
3.5
4
3
4
5
6
7
8
9

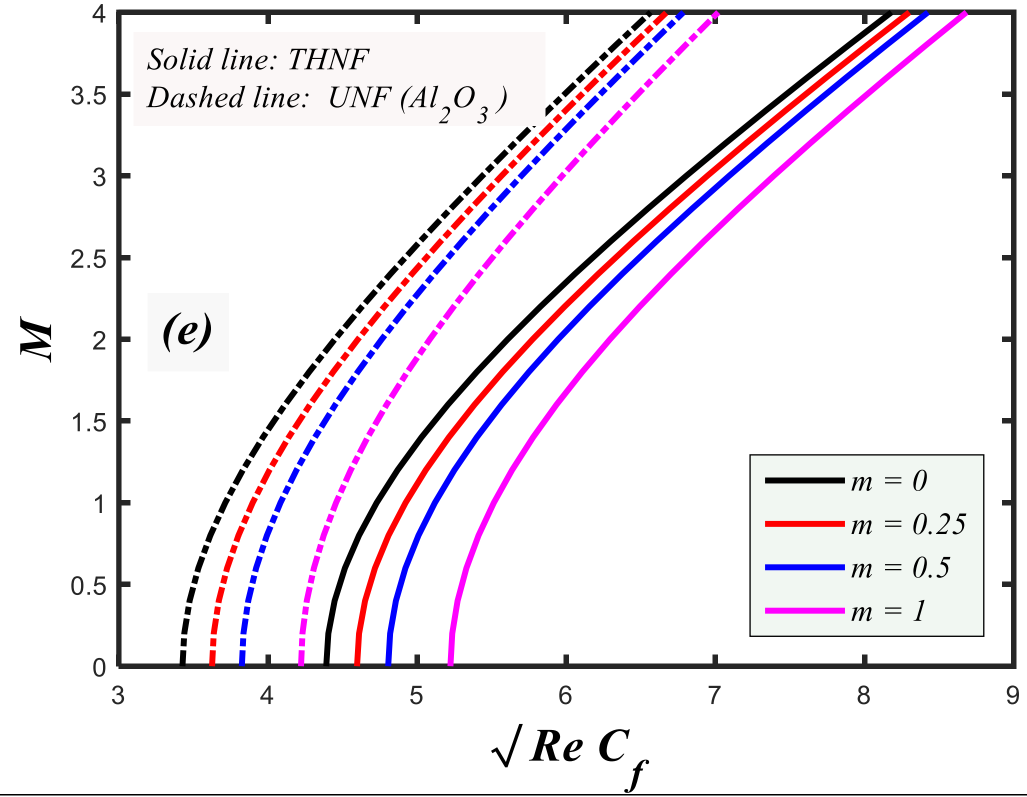
Solid line: THNF
Dashed line: UNF (Al_2O_3)
(e)
M
$\sqrt{Re}\, C_f$
m = 0
m = 0.25
m = 0.5
m = 1
0
0.5
1
1.5
2
2.5
3
3.5
4
3
4
5
6
7
8
9

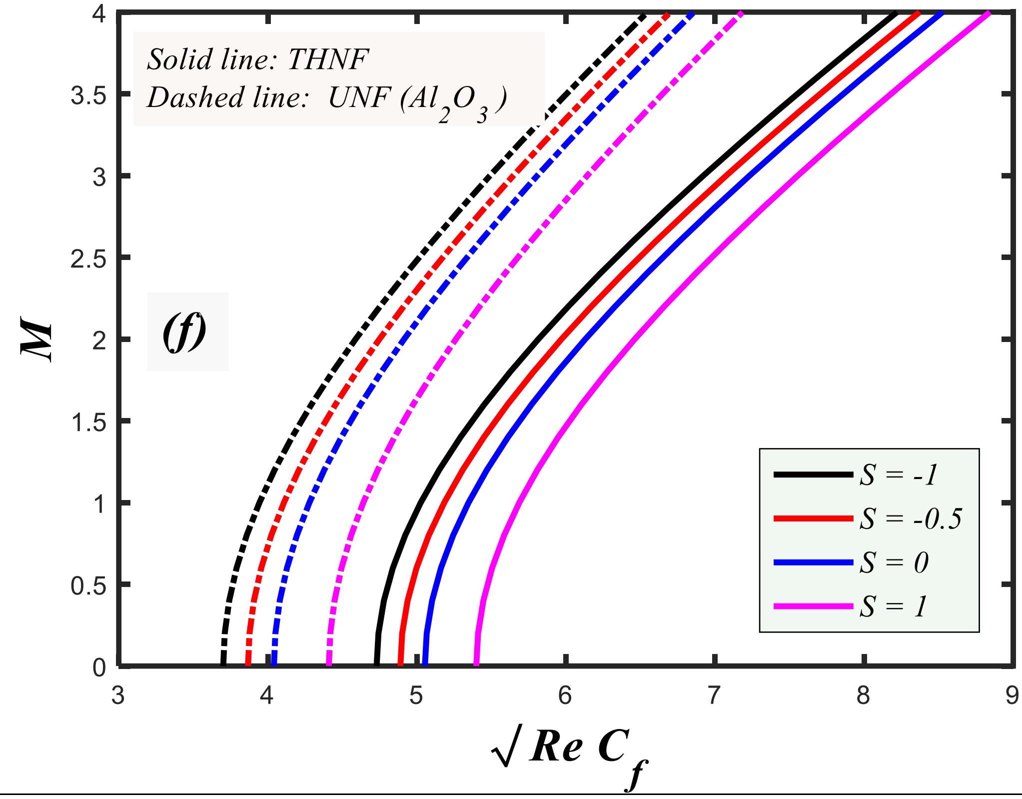
Solid line: THNF
Dashed line: UNF (Al_2O_3)
(f)
M
$\sqrt{Re}\, C_f$
S = -1
S = -0.5
S = 0
S = 1
0
0.5
1
1.5
2
2.5
3
3.5
4
3
4
5
6
7
8
9

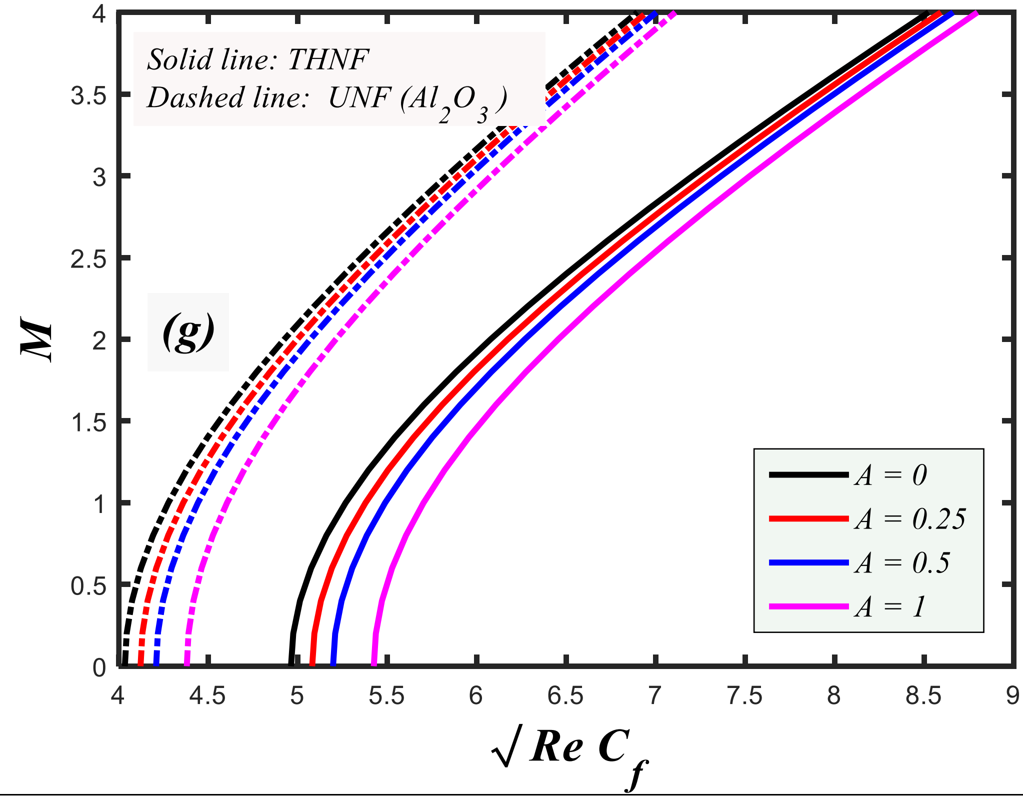
Solid line: THNF
Dashed line: UNF (Al_2O_3)
(g)
M
$\sqrt{Re}\, C_f$
A = 0
A = 0.25
A = 0.5
A = 1
0
0.5
1
1.5
2
2.5
3
3.5
4
4
4.5
5
5.5
6
6.5
7
7.5
8
8.5
9

Figs. 4. Impacts of (a)Zeta potential parameter, (b) Electroosmosis parameter, (c) rheological power-law index, (d) Forchheimer number, (e) Falkner-Skan power-law constant, (f) suction/ injection parameter and (g) unsteadiness parameter, on surface friction coefficients for fixed value of $\kappa = 1; m = 0.3; U_E = 2; n = 0.2; We = 0.1; Fr = 0.25; M = 2; Da = 0.5; A = 1; S = 0.5; \xi = 1, \gamma = 0.2, \phi_1 = 0.03; \phi_2 = 0.02; \phi_1 = 0.01$.

The $f'(\eta)$ velocity profiles for both THNF and UNF are displayed for a range of Forchheimer numbers in Fig. 2(b). As can be observed, in the case of a Darcian porous medium for which second order inertial drag effects vanish $(F_r = 0)$ and the Forchheimer drag force term $Fr(f'^2 - 1)$ vanishes. This produces the maximum velocity magnitudes for both THNF and UNF. With increment in Fr, $f'(\eta)$ is significantly reduced. However again higher velocity magnitudes are achieved with UNF case relative to the THNF at any value of Forchheimer number. Therefore, greater retardation is induced in the THNF case with larger Forchheimer number and a thicker momentum boundary layer is generated at the wedge surface. The (alumina nanoparticle) unary nanofluid may experience less drag due to the modification in viscosity at lower volume fraction present compared with ternary nanofluid. It is also noteworthy that negative velocity is generated very close to the wedge surface indicating that Forchheimer effect produces a weak backflow (flow reversal) in the vicinity of the wall.

In Fig.2(c), for both THNF and UNF, the impacts of varying the wedge parameter γ on the velocity distribution is illustrated. It is clear that when the wedge parameter is increased positively i. e. *contracting wedge* case ($\gamma = 0.25, 0.5$), the velocity magnitude is decreased. However, with negative increment in wedge parameter ($\gamma = -0.25, -0.5$) which implies *wedge stretching* the reverse trend is induced and the velocity is enhanced. The intermediate case of a stationary wedge naturally falls between the other two stretching and contracting wedge cases. The presence of surface stretching on the wedge assists in momentum development in the boundary layer which is reduced in thickness and results in significant flow acceleration. The contracting surface destroys momentum in the boundary layer which manifests in deceleration and a greater momentum boundary layer thickness. Again, significantly greater velocity is computed for the UNF case relative to the THNF case.

Fig. 2(d) illustrates the influence of the wedge angle parameter, *m*, on velocity evolution. The velocity of the fluid is substantially reduced as *m* rises. A physical increase in the wedge angle parameter reduces the pressure exerted on the fluid. Even more so, the velocity profile is more sensitive to variations in m values at intermediate distance from the wedge surface, with a lesser influence at the wedge surface (wall) and in the free stream. The parameter, $m = \frac{\beta}{2-\beta}$ is also known as the Hartree pressure gradient parameter. Here $\beta = \Omega/\pi$ for a vertex angle Ω of the wedge. The case $m = 0$ implies Blasius boundary layer flow along a flat horizontal surface (for which $\beta = 0$ *and the wedge morphs into a flat plate)* and $m = 1$ corresponds to *forward stagnation point boundary layer flow* adjacent to a vertical surface (i. e. $\beta = 1$ *such that the wedge angle* $\Omega = \pi$ *implying that the wedge has morphed into a vertical plate).* Both these scenarios are also of interest in materials processing operations e. g. stretching/contracting sheet processes. The case of m = 2 implies that β =4/3 so that the internal wedge apex angle = *4 π/3 ie. 240 degrees. This corresponds to the case of the reverse wedge configuration i. e. backward facing wedge.* Clearly as wedge internal angle is increased, the resistance to the boundary layer flow is increased. The maximum velocity therefore corresponds to the case $m = 0$ and the minimal velocity to $m = 2$. The momentum boundary layer thickness will be minimized and maximized respectively for these two cases. The geometric nature of the wedge will therefore exert a profound influence on velocity development in the boundary layer and can be exploited to achieve desired flow control in nanomaterials operations [5]. It is also pertinent to note once again that markedly greater velocity (and lower hydrodynamic boundary layer thickness) is computed for the UNF case (alumina single nanoparticle) compared with the THNF case, and again the disparity is highest at intermediate distance transverse to the wedge surface.

Fig. 2(e) shows the effect of tangent hyperbolic power-law index (n) on the velocity distribution.

For both THNF and UNF, the rheological nature has significant effects on the distribution of fluid velocities in the boundary layer, although again the UNF case exhibits considerably greater velocity magnitudes. A shear thickening nanofluid (dilatant) has $n > 1$, a shear thinning nanofluid has $n < 1$ and for the classical Newtonian viscous case, $n = 1$. Figure 2(e) reveals that as n increases, the velocity profile exhibits a declining trend. The flow is strongly decelerated for dilatant behaviour and momentum boundary layer thickness is elevated. The considerable increase in viscosity associated with shear-thickening is responsible for the retarding behaviour. It has been shown experimentally that the increment in nanofluid viscosity for dilatant power-law nanofluids increases with a reduced concentration of nanoparticles (volume fraction) [43]. The combination of 3 nanoparticles in the THNF will also hike the nanoparticle concentrations which will boost viscous forces in the nanofluid and lead to deceleration in the boundary layer flow. Clearly there is a significant deviation between shear-thinning, shear-thickening and Newtonian nanofluid velocity profiles, confirming that the Newtonian model either under-predicts or over-predicts velocity magnitudes and is therefore inadequate for realistic coating applications.

Fig. 2(f) visualizes the influence of wedge surface transpiration parameter, S on the dimensionless velocity profile $f'(\eta)$ again for both the THNF and UNF cases. As the injection parameter S increases positively $(S > 0)$, the fluid velocity is enhanced, and momentum boundary layer thickness is reduced. THNF velocity magnitudes are exceeded by the UNF case. The introduction of nanofluid via the perforated wedge surface into the boundary layer adds momentum to the flow (blowing). This induces acceleration. The reverse trend is computed with increasing surface suction $(S < 0)$ wherein nanofluid is extracted via the wedge surface from the boundary layer inducing stronger adherence to the wall and an associated deceleration effect. Strong suction therefore produces a thicker momentum boundary layer. The solid wall (non-porous wedge surface) case i. e. S= 0 achieves velocity magnitudes intercalated between the suction and injection cases. Significant manipulation of the coating tangent hyperbolic nanofluid regime is therefore achieved with the mechanism of wall lateral mass flux (porous wedge surface).

Fig. 2(g) displays the evolution in velocity $f'(\eta)$ with variation in Weissenberg number (We) on for both THNF and UNF cases. With increment in We there is a decrement in velocity throughout the boundary layer transverse to the wedge surface. Noticeably greater velocity magnitudes are computed for UNF relative to THNF. $We = \frac{\Gamma\, U_e^{\frac{3}{2}}}{\sqrt{\nu_f x}}$ and expresses the ratio of elastic force in the rheological nanofluid to the viscous force. This parameter features only in the higher order shear term in Eqn. (23) i. e. $A_\nu f'''\left((1+n) + nWe\sqrt{1+m}\, f''\right)$ unlike the power-law rheological index which appears in multiple terms. For We <1, the viscous force will dominate the elastic force, and this will generate stronger resistance to the flow, manifesting in boundary layer deceleration. Weissenberg number also expresses the ratio of the fluid relaxation and retardation times. The tangent hyperbolic model is an *elastico-viscous model,* which combines elastic and viscous properties. When the time scale (retardation time) of a flow is significantly lower than the relaxation time in the nanofluid, elastic effects dominate, and this corresponds to We > 1. However, in practical rheological nano-coating flows [39, 44], the case of We <1 is more appropriate in which retardation time significantly exceeds the relaxation time and elastic effects relax sufficiently for viscous effects to dominate. Therefore, we have restricted attention to the case of We <1.

Fig.2(h) visualizes the effect of electric field parameter (U_E) on dimensionless velocity distributions $f'(\eta)$ for both THNF and UNF systems. These distributions are shown for both positive and negative values of U_E. For robust flow control on the wedge, the electric field plays an extremely significant role. The parameter value of the electrical field is negative when the electrical field direction is reversed and oriented in the positive axial direction, while it is positive when oriented in the negative axial direction. It is evident that a positive increase in the value of U_E results in an increase in the flow velocity (and decrease in hydrodynamic boundary layer thickness of the tangent hyperbolic nanofluid) whereas the contrary effect is induced for negative U_E. The vanishing electric field case corresponds to $U_E = 0$. Significantly higher velocities are observed for the UNF case compared to the THNF case, at all values of U_E.

Influences of M on $f'(\eta)$ is presented in Fig.2(i) for both THNF and UNF cases. The magnetic field may be thought of as the ratio of the forces exerted by electromagnetic fields to those exerted by viscous fields. As a direct result of this, the increase in the magnetic field acted to slow down the movement of the liquid. It can be seen rather clearly from this graphic that the momentum barrier layer will get thinner as M increases. It is a well-established fact that as the value of the Hartmann number M increases, the velocity profile, denoted by $f'(\eta)$, will inevitably get flatter. This phenomenon may be explained by the fact that the Lorentz force is intensified owing to bigger values of the magnetic field which elevate the Hartmann number for both THNF and UNF cases. As a consequence of this strengthening, it generates resistance in the flow of the fluid. The UNF scenario has much larger velocities than the THNF case.

Figs.3(a) and 3(b), respectively, illustrate the non-dimensional electric potential profiles $\phi(\eta)$ as a function of zeta potential parameter (ξ) and electroosmosis parameter (κ) in the case of $m = 0$ (Blasius boundary layer flow along a flat horizontal surface) and $m = 1$ (*forward stagnation point boundary layer flow* adjacent to a vertical surface). Significantly higher electrical potential values are computed for $m = 0$ compared with $m = 1$. There is also a marked enhancement in electric potential magnitudes with increment in zeta potential parameter. Zeta potential is the charge developing at the interface between the wedge surface and the tangent hyperbolic ionic magnetic nanofluid. It is typically of the order of milli-Volts. It modifies the net charge at the particle surface and therefore influences the ion distribution in the nearby region, increasing the concentration of counterions close to the wedge surface. Thus, an electrical double layer is formed in the region of the particle-nanofluid interface. The double layer has two section- *an interior zone* which includes ions bound closely to the wall (wedge face) and an *external zone* where a balance of electrostatic forces and random thermal motion dictates ion distribution. The electrical potential in this region, therefore, decays with increasing distance from the surface until, at a critical distance, it attains the so-called bulk solution value, which is nominally zero. The zeta potential is effectively the electrical potential value at the wedge surface. Zeta potential is therefore a function of the surface charge of the particle, any adsorbed layer at the interface, and the nature and composition of the engulfing tangent hyperbolic nanofluid. In industrial operations, zeta potential can be used to control of colloidal stability and flocculation processes. Electric potential distribution is found to be maximal at the non-zero wedge angle (i. e. forward stagnation flow case, $m = 1$). Conversely a significant suppression in electrical potential is computed with increment in electroosmosis parameter (κ) as observed in Fig. 3(b). However again higher magnitudes correspond to the vertical surface case ($m = 1$) and much lower magnitudes arise for the Blasius horizontal plate case ($m = 0$). It is also apparent that there is no variation in electrical potential values at the wedge surface with electroosmosis parameter variation (κ) whereas in Fig. 3(a) there is a significant variation at the wall with changes in the zeta potential parameter.

Figs. 4(a) – 4(g) depicts the influence of zeta potential parameter(ξ), electroosmosis parameter(κ), rheological power-law index (n), Forchheimer number (Fr), Falkner-Skan power-law wedge constant (m), suction/injection parameter (S) and unsteadiness parameter (A) on surface friction coefficient $\sqrt{Re}C_f$ for both THNF and UNF cases.

Figs.4(a-b) visualize the variation of surface friction coefficients $\sqrt{Re}f''(0)$ for different value of zeta potential (ξ) and electroosmosis (κ) parameters against Hartmann (magnetic) number M with THNF and UNF. Skin friction is significantly boosted with increasing Hartmann number. Similarly, there is a significant boost in skin friction with increasing zeta potential parameter. THNF achieves much higher skin friction than the UNF case. The ξ and κ parameters can be exploited to therefore substantially modify characteristics on the wedge surface and manipulate boundary layer behavior. The skin friction coefficient values are higher for THNF than UNF in both Figs. 4a, b. A high zeta potential and electro-osmotic parameter both generate greater electric field force and pressure in the EDL which produces flow acceleration. Figure 4(c) shows that a rise in *n* produces a depression in skin friction $\sqrt{Re}C_f$ since higher viscosity is associated with dilatant nanofluids relative to pseudoplastic nanofluids. Again, higher skin friction arises for THNF compared with UNF. It is also evident that negative skin friction is associated with the dilatant case (n >1) whereas positive skin friction is produced with pseudoplastic nanofluids (n <1). For pseudoplastic nanofluids there is an upward trend in skin friction with increasing magnetic parameter whereas for dilatant nanofluids there is a downward trend with greater magnetic parameter. Fig. 4(d) portrays the variation of $\sqrt{Re}C_f$ with Forchheimer number (Fr). A strong decrement in skin friction is induced with greater Fr values since significant quadratic drag is produced. The case of the Darcy medium $(Fr = 0)$ achieves the highest skin friction magnitudes at all values of magnetic parameter, M. THNF achieves much greater skin friction than UNF. The surface viscous drag $\sqrt{Re}C_f$ is strongly modified therefore for both THNF (black solid line) and UNF (black dotted line) for different values of Fr and magnetic parameter, M. Fig.4(e) shows that with increasing wedge parameter, *m* and magnetic parameter, *M*, there is a significant enhancement of $\sqrt{Re}C_f$ for both THNF and UNF, although again THNF produces higher magnitudes. Fig. 4(f) indicates that with increasing surface suction $(S < 0)$ for both THNF and UNF cases, there is a reduction in skin friction, whereas there is a strong monotonic increment with increasing magnetic parameter, *M*. THNF however produces much greater magnitudes than UNF. A substantial boost in skin friction is as expected induced with greater surface injection i. e. blowing at the wedge face (S >0). Finally in Fig. 4(g) it is apparent that with an increase in the unsteadiness parameter, *A*, and magnetic parameter, *M*, there is a marked enhancement in skin friction for both THNF and UNF cases. As before, the THNF case attains significantly greater skin friction magnitudes than the UNF case. The minimal skin friction is therefore associated effectively with the steady case (A = 0) and vanishing magnetic field (M = 0) and associated with the UNF (alumina nanoparticle) case.

6. CONCLUSIONS

An analytical and numerical study has been presented for unsteady, electro-magneto-hydrodynamic (EMHD) incompressible, two-dimensional tangent hyperbolic non-Newtonian ternary hybrid nanofluid boundary layer coating flow external to a 2-dimensional wedge geometry adjacent to a non-Darcy porous medium. The effects of zeta-potential and surface suction/injection have been included. The Darcy-Forchheimer drag force model is deployed. The ternary composite nanofluid (THNF) considered comprises three nanoparticles (Al_2O_3, TiO_2 and SiO_2) with aqueous base fluid (H_2O). The unitary nanofluid (UNF) utilizes only Al_2O_3 nanoparticles in water. The governing conservation partial differential equations for continuity and momentum and associated boundary conditions at the wedge surface and free stream are transformed with appropriate similarity variables. The emerging ordinary differential nonlinear boundary value problem is numerically solved in MATLAB with the bvpc collocation technique. Validation with earlier studies is included. The computations have shown that:

(i) Increasing Darcy number and surface injection parameter contribute to an increase in velocity and reduction in momentum boundary layer thickness.

(ii) Increasing zeta potential and electroosmosis parameters elevate skin friction coefficient for both THNF and UNF cases.

(iii) A significant deceleration is induced in the flow of a ternary hybrid nanofluid with an increase in the electric field parameter.

(iv) An increment in Falkner-Skan power-law constant (moving wedge angle parameter) boosts the local skin friction coefficient for both the ternary hybrid nanofluid (THNF) and unitary Al_2O_3 nanofluid (UNF) cases.

(v) Both electroosmosis and electric field parameters improve the velocity distribution for both THNF and UNF flow cases.

(vi) An increment in tangent hyperbolic power-law rheological parameter (from shear-thinning $n < 1$ to shear-thickening $n > 1$) decelerates the flow.

(vii) Increasing Forcheimmer number (non-Darcy inertial drag) and greater Weissenberg number induce strong flow deceleration (thicker momentum boundary layers).

(viii) Higher values of wedge surface injection parameter accelerate the flow and decrease momentum boundary layer thickness whereas surface suction produces the opposite effect.

(ix) With increasing zeta potential parameter electric potential magnitudes are elevated.

(x) With an increase in the unsteadiness parameter and magnetic body force parameter there is a marked enhancement in skin friction for both THNF and UNF cases.

(xi) Electric potential distribution is found to be maximal for non-zero wedge angle (i. e. forward stagnation flow case, $m = 1$).

(xii) A marked depletion in electrical potential is computed with increment in electroosmosis parameter and much higher values are observed for the vertical surface case (m =1) and much lower magnitudes arise for the Blasius horizontal plate case ($m = 0$).

(xiii) There is no variation in electrical potential values at the wedge surface with electroosmosis parameter variation whereas there is a significant variation at the wall with changes in the zeta potential parameter.

The present study has revealed some intriguing features of non-Newtonian electro-magneto-hydrodynamic coating flow on a wedge body. The tangent hyperbolic rheological model has been used. Future studies may consider alternative non-Newtonian models such as the micropolar model [21, 29] and will be explored soon. Additionally, wall slip, Joule heating [48] and non-Fourier heat flux [49] may also be considered in subsequent investigations.

APPENDIX

The sample Matlab BVP4C function code for the proposed mathematical model is extracted as follows:

```
function Sample_parameter
global K m A UE Ar Av n We Be M1 Da As S Ga xi Fr


K = 1; m = 0.3; Be = 2*m/(1+m);  UE = 2; n = 0.2;We = 0.1;
Fr = 0.5; M1 = 2; Da= 0.5; A = 1; xi = 01; S = 0.5; Ga = .2;
P1=0.08;P2=0.0;P3=0.0; P=P1+P2+P3; B1=37.1;C1=612.6; B2=13.5;C2=904.4;
B3=2.5;C3=6.2; rf=997.1;rf1=3970;rf2=4250;rf3=3970;
```

```
Sf=5.5*10^(-6);Sf1=35*10^6;Sf2=3.5*10^6;Sf3=10^(-23);
a1=((1+B1*P+C1*P^2)*P1+(1+B2*P+C2*P^2)*P2+(1+B3*P+C3*P^2)*P3)/P;
Ar=(1-P)+((rf1*P1+rf2*P2+rf3*P3)/rf); Av=a1/Ar;
Snf = Sf*(((1+2*P3)*Sf3+(1-2*P3)*Sf)/((1-P3)*Sf3+(1-2*P3)*Sf));
Shnf = Snf*(((1+2*P3)*Sf2+(1-2*P3)*Snf)/((1-P3)*Sf2+(1-2*P3)*Snf));
Sthnf = (Shnf/Sf)*(((1+2*P3)*Sf1+(1-2*P3)*Shnf)/((1-P3)*Sf1+(1-2*P3)*Shnf));
As=Sthnf;
xlow=0; xhigh=8; xint= linspace(xlow,xhigh,41);
options = bvpset('RelTol',1e-9,'Stats','on');
solinit= bvpinit(linspace(xlow,xhigh,41),ones(5,1));
sol = bvp4c(@bvp4ode,@bvp4bc,solinit,options);
Sxint= deval(sol,xint);
plot(xint,Sxint(2,:),'m-*', 'LineWidth',2.2)

function dydx= bvp4ode(x,y)
global K m A UE Ar Av n We Be M1 Da As Fr
dydx =[ y(2)
    y(3)
    ((((As*M1*M1+Av*Ar*Da)*(y(2)-1))/(Ar*(1+m)))-(A/(1+m))*(2-y(3)*x-2*y(2))-y(1)*y(3)-Fr*(y(2)*y(2)-1)-
Be*(1-y(2)*y(2))-(UE*K*K/Ar)*sinh(y(4)))/(Av*((1+n)+n*We*y(3)*sqrt(1+m)))
    y(5)
    (K/(1+m))*sinh(y(4))];

  function res = bvp4bc(ya,yb)
global S Ga m xi
res = [ ya(1)-(S/(1+m))
    ya(2)+Ga
    yb(2)-1
    ya(4)-xi
    yb(4)];
```

REFERENCES

1. Hsu, C.C. 1967. “Viscoelastic flow past a wedge with a soluble coating.” J. Fluid Mechanics, 27:445-463.

2. Al-Anazi D, Hashmi M.S.J. and Yilbas, B.S. 2007. “High-velocity oxy-fuel thermally sprayed CoNiCrAlY coatings on Ti-6Al-4V alloy: High cycle fatigue properties of coating.” Proceedings of the Institution of Mechanical Engineers, Part B: Journal of Engineering Manufacture, 221(4): 647-654.
3. Jiang W., et al. 2019. ”Wear resistance of Ni-Co/SiC composite coating by jet electrodeposition in the presence of magnetic field, Proceedings of the Institution of Mechanical Engineers.” Part B: Journal of Engineering Manufacture, 234(3): 431-438.
4. Reddy U.M., et al. 2014. “Experimental investigation to study the effect of electrostatic micro-solid lubricant–coated carbide tools on machinability parameters in turning.” Proc IMechE, Part B: J Engineering Manufacture, 229:5. .
5. Hussain C.M. Thomas, S. 2020. “Handbook of Polymer and Ceramic Nanotechnology.” Springer International Publishing, Cham.
6. Feng Q., et al. 2007. “Preparation of nanostructured Ni/Al2O3 composite coatings in high magnetic field.” Surface and Coatings Technology, 201(14): 6247-6252.
7. Barletta M., and Tagliaferri, V. 2006. “Influence of process parameters in electrostatic fluidized bed coating.” Surface and Coatings Technology, 200(14/15): 4619-4629.
8. Zhai L.L., et al. 2019. “Microstructure, microhardness and corrosion resistance of NiCrBSi coatings under electromagnetic field auxiliary laser cladding.” Surface and Coatings Technology, 358:531-538.
9. Liu X., et al. 2016. “Jet electrodeposition of nanocrystalline nickel assisted by controllable friction.” Surface and Coatings Technology, 305:231-240.
10. Faruk Oytun and Umut Ugur Ozkose, 2019. “Preparation and characterization of electrically conductive multiwalled carbon nanotube/polyoxazoline nanocomposite films using spray coating.” Journal of Coatings Technology and Research, 16:1757–1764.
11. Mostafaei, A., and Farzad Nasirpouri. 2013. “Preparation and characterization of a novel conducting nanocomposite blended with epoxy coating for antifouling and antibacterial applications.” Journal of Coatings Technology and Research, 10: 679–694.
12. M.R. Islam M.R. et al. 2020. “Rheological and antimicrobial properties of epoxy-based hybrid nanocoatings.” Polymer Testing, 81:106202.

13. Palza H., Quijada R., and Delgado K. 2015. “Antimicrobial polymer composites with copper micro and nanoparticles: effect of particle size and polymer matrix.” J. Bioact. Compat Polym. 30(4): 1-15.
14. Parameswaranpillai J., George A., Pionteck J. and Thomas S. 2013. “Investigation of cure reaction, rheology, volume shrinkage and thermomechanical properties of nano-TiO2 filled epoxy/DDS composites, J. Polym., 2013 | Article ID 183463 | https://doi.org/10.1155/ 2013/183463.
15. Nguyen D.H., Song G.S. and Lee, D.S. 2011. “Effects of colloidal nanosilica on the rheological properties of epoxy resins filled with organoclay.” J. Nanosci. Nanotechnol., 11:4448-4451.
16. Zhang M., et al., 2021. “A nano-micro engineering nanofiber for electromagnetic absorber, green shielding and sensor.” Nano-Micro Letters, 13: 27.
17. Yan J., Huang Y., Zhang Z., Liu X.D. 2019. “Novel 3D micro-sheets contain cobalt particles and numerous interlaced carbon nanotubes for high-performance electromagnetic wave absorption.” J. Alloys Comp., 785:1206-1214.
18. Garg V.K., and Rajagopal, K.R. 1991. “Flow of a non-Newtonian fluid past a wedge.” Acta Mechanica, 88:113–123.
19. Kudenatti R.B., et al., 2022. “Stability of hydromagnetic boundary layer flow of non-Newtonian power-law fluid flow over a moving wedge.” Engineering with Computers, 38:1107–1126.
20. Abdul Gaffar S., Prasad V.R., Vijaya B., and Anwar Bég, O. 2015. “Mixed convection flow of magnetic viscoelastic polymer from a non-isothermal wedge with Biot number effects.” Int. J. Eng. Math., 2015:1-15.
21. Anwar Bég O., Vasu B., Ray A.K., , Bég, T.A., Kadir A., Leonard H.J., and Gorla R.S.R. 2020. “Homotopy simulation of dissipative micropolar flow and heat transfer from a two-dimensional body with heat sink effect: applications in polymer coating.” Chem. Biochem. Eng. Quart., 34:257-275.
22. Malik M.Y., Salahuddin T., Hussain A., and Bilal S. 2015. “MHD flow of tangent hyperbolic fluid over a stretching cylinder: using Keller box method.” Journal of Magnetism and Magnetic Materials, 395:271–276.

23. Kumar K.G., Gireesha B.J.,, and R. S. R. Gorla R.S.R. 2018. “Flow and heat transfer of dusty hyperbolic tangent fluid over a stretching sheet in the presence of thermal radiation and magnetic field.” International Journal of Mechanical and Materials Engineering, 13:2.
24. Gharami P.P., Reza-E-Rabbi S., Arifuzzaman S.M., Khan M.S., Sarkar T., and Ahmmed S.F.2020. “MHD effect on unsteady flow of tangent hyperbolic nano-fluid past a moving cylinder with chemical reaction”, SN Applied Sciences, 2(7):1256.
25. Hayat T., Ullah,I., Alsaedi A. and Ahmad B.2017. “Modeling tangent hyperbolic nanoliquid flow with heat and mass flux conditions.” Eur. Phys. J. Plus, 132(3):1–15.
26. Khan S.U., et al. 2019. “Theoretical analysis of tangent hyperbolic nanoparticles with combined electrical MHD, activation energy and Wu's slip features: a mathematical model.” Phys. Scr. 94:125211.
27. Thameem Basha H., Sivaraj R., Prasad V.R and Anwar Bég O. 2021. “Entropy generation of tangent hyperbolic nanofluid flow over a circular cylinder in the presence of nonlinear Boussinesq approximation: A non-similar solution.” J. Thermal Analysis and Calorimetry, 143:2273–2289.
28. Prakash J., Tripathi D., Akkurt N. and Anwar Bég O. 2022. “Tangent hyperbolic non-newtonian radiative bioconvection nanofluid flow from a bi-directional stretching surface with electro-magneto-hydrodynamic.” Joule heating and modified diffusion effects, European Physical Journal Plus. 137: 472. doi.org/10.1140/epjp/s13360-022-02613-x
29. Umavathi J.C. 2022. “Electrically-conducting micropolar nanofluid with heat source/sink over a wedge: Ion and Hall currents.” Journal of Magnetism and Magnetic Materials, 559: 169548.
30. Ali L., et al., 2022. “A comparative study of unsteady MHD Falkner–Skan wedge flow for non-Newtonian nanofluids considering thermal radiation and activation energy.” Chinese Journal of Physics, 77:1625-1638.
31. Ali B., et al., 2021. “Finite element study for magnetohydrodynamic (MHD) tangent hyperbolic nanofluid flow over a faster/slower stretching wedge with activation energy.” Mathematics 9(1):25. https://doi.org/10.3390/math9010025
32. Bhatti M.M., Anwar Bég O., Ellahi R. and Abbas T. 2022. “Natural convection non-Newtonian EMHD dissipative flow through a microchannel containing a non-Darcy porous

medium: homotopy perturbation method study." Qualitative Theory of Dynamical Systems, 21:97.

33. Haider F., et al., 2021. "Flow of hybrid nanofluid through Darcy-Forchheimer porous space with variable characteristics." Alexandria Engineering Journal, 60:3047-3056.
34. Kandasamy R., Muhaimin I. and Rosmila A.K. 2014. "The performance evaluation of unsteady MHD non-Darcy nanofluid flow over a porous wedge due to renewable (solar) energy." Renewable Energy, 64:1-9.
35. Zhu H., Lin Y. and Yin Y. 2004. "A novel one-step chemical method for preparation of copper nanofluids." Journal of Colloid and Interface Science, 277:100-103.
36. Masuda S., Nagao M., Takahaty K., Konoshi Y., Gallyas F, Tabira T. and Sasaki R. 1993. "Functional erythropoietin receptor of the cells with neuronal characteristics". Journal of Biological Chemistry, 268:11208-11216.
37. Lee S., Choi S.U.S., S. Li S. and Eastman J.A. 1999. "Measuring thermal conductivity of fluids containing oxide nanoparticles". Trans. ASME J. Heat Transfer, 121:280-289.
38. Eastman J.A., Choi S.U.S., Li S., Yu W., and Thompson L.J. 2001. "Anomalous increased effective thermal conductivities of ethylene glycol-based nanofluids containing copper nanoparticles." Applied Physics Letters, 78:718-720.
39. Hussain C.M. 2018. Handbook of Nanomaterials for Industrial Applications, Elsevier, USA.
40. Umavathi J.C., Patil S.L., Mahanthesh B. and Anwar Bég O. 2021. "Unsteady squeezing flow of magnetized nano-lubricant between parallel disks with Robin boundary condition." Proc. IMechE J. Nanomaterials, Nanoengineering, Nanosystems,235(3-4):1-15. DOI: 10.1177/23977914211036562 (15 pages)
41. Kattan P.I. 2008. "Matlab for Beginners", Create Space Independent Publishing Platform, USA.
42. White F.M. 2006. "Viscous Fluid Flow", 3rd ed. New York: McGraw-Hill.
43. Hojjat M., Etemad S.Gh., Bagheri R. and Thibault J. 2011. "Rheological characteristics of non-Newtonian nanofluids: Experimental investigation." International Communications in Heat and Mass Transfer, 38:144–148.
44. Vajtai R. 2013. (Ed), "Springer Handbook of Nanomaterials". Springer-Verlag, Germany.

45. Sarangi M.K., Thatoi D.N., Nayak M.K., Prakash J., Ramesh K. and Azam M. 2022, “Rotational flow and thermal behavior of ternary hybrid nanomaterials at small and high Prandtl numbers”. International Communications in Heat and Mass Transfer 138:106337.
46. Shampine, L.F., and Kierzenka J. 2001. "A BVP Solver based on residual control and the MATLAB PSE." ACM Trans. Math. Softw. 27(3):299–316.
47. Shampine, L.F., Reichelt M.W. and J. Kierzenka J. 2004. "Solving Boundary Value Problems for Ordinary Differential Equations in MATLAB with bvp4c”. MATLAB File Exchange.
48. A. Mishra and M. Kumar, Velocity and thermal slip effects on MHD nanofluid flow past a stretching cylinder with viscous dissipation and Joule heating, *SN Applied Sciences* volume 2, Article number: 1350 (2020).
49. H. Upreti and A. Mishra, The performance evolution of hybrid nanofluid flow over a rotating disk using Cattaneo–Christov double diffusion and Yamada–Ota model, *Waves in Random and Complex Media* (2022). doi.org/10.1080/17455030.2022.2147243